Research Square

Preprints are preliminary reports that have not undergone peer review.
They should not be considered conclusive, used to inform clinical practice,
or referenced by the media as validated information.

Winter 2026/27 and the Emerging Super El Niño: A Prospective Diagnosis of North American Atmospheric Teleconnections

Fatemeh Moradi

University of Naples Federico II: Universita degli Studi di Napoli Federico II

Hossein Bonakdari

hbonakda@uottawa.ca

Ottawa University https://orcid.org/0000-0001-6169-3654

Research Article

Keywords: El Niño–Southern Oscillation, ENSO extremes, Pacific Decadal Oscillation, atmospheric teleconnections, seasonal predictability, North America

Posted Date: November 6th, 2026

DOI: https://doi.org/10.21203/rs.3.rs-11339395/v1

License: This work is licensed under a Creative Commons Attribution 4.0 International License.
Read Full License

Winter 2026/27 and the Emerging Super El Niño: A Prospective Diagnosis of North American Atmospheric Teleconnections

Fatemeh Moradi[a,b], Hossein Bonakdari[a,*]

[a]Department of Civil Engineering, University of Ottawa, 161 Louis Pasteur Private, Ottawa, ON, K1N 6N5, Canada

[b]Department of Civil, Building and Environmental Engineering (DICEA), University of Naples Federico II, Naples, Italy

[*]Corresponding author: Hossein Bonakdari; E-mail: hbonakda@uottawa.ca; ORCID: https://orcid.org/0000-0001-6169-3654

Abstract

Very strong El Niño events are rare, limiting statistical assessment of their atmospheric teleconnections and seasonal persistence, especially under unusual Pacific background conditions. This study examines the developing 2026 event using six climate indices and observations available through August 2026. An integrated framework combines historical ranking of El Niño–Southern Oscillation (ENSO) intensification, joint Niño-3.4–Pacific Decadal Oscillation (PDO) state analysis, dependence-aware teleconnection testing, PDO interaction modelling and expanding-window hindcasting with explicit assessment of the historical predictor range. Monthly circular-shift tests, seasonal block permutations with false-discovery-rate adjustment and heteroskedasticity- and autocorrelation-consistent (HAC) regression were used to evaluate circulation relationships and PDO modulation. The August 2026 monthly Niño-3.4 anomaly reached +2.55 °C and the June–August (JJA) mean +2.12 °C; the March–August increase of +2.52 °C ranked first among 45 developing years. Despite this exceptional warming, the March–July PDO averaged −1.53, and the July joint state (three-month Niño-3.4 = +2.12 °C; PDO = −1.73) was absent from the preceding record under the specified thresholds. Winter Pacific–North American (PNA) correlations with developing-year JJA, September–November and concurrent December–February Niño-3.4 were 0.55, 0.59 and 0.56, whereas North Atlantic Oscillation and Arctic Oscillation associations were not significant after multiple-testing adjustment. The ENSO–PNA relationship was robust to event exclusion and block-bootstrap resampling, but PDO modulation was not detected (HAC $p = 0.174$). Historical JJA-to-winter persistence achieved an expanding-window hindcast R^2 of 0.74 across 29 predictions; however, the 2026 summer anomaly exceeded the historical calibration maximum by 0.75 °C ($\delta = 0.25$), making the nominal winter estimate of +2.99 °C an unvalidated extrapolation. The main contribution is to distinguish an unprecedented observed ENSO–PDO configuration from robust historical circulation associations and to assess their uncertain transferability beyond the calibration domain, providing a prospective benchmark for evaluating winter 2026/27 without equating historical statistical skill with reliable prediction under exceptional conditions.

Keywords: El Niño–Southern Oscillation; ENSO extremes; Pacific Decadal Oscillation; atmospheric teleconnections; seasonal predictability; North America

1. Introduction

The El Niño–Southern Oscillation (ENSO) is a dominant mode of interannual climate variability in the tropical Pacific and an important source of seasonal predictability for Northern Hemisphere winter climate (Timmermann et al., 2018; Yeh et al., 2018). Anomalous warming of the central and eastern equatorial Pacific alters tropical deep convection, generating upper-tropospheric divergence and exciting quasi-stationary Rossby waves that propagate across the North Pacific and North America (Scaife et al., 2017; Taschetto et al., 2020). The Pacific–North American (PNA) pattern is a major atmospheric expression of this teleconnection. Its positive phase is associated with a deepened Aleutian low, an amplified ridge over western North America, and a trough over the southeastern United States (Deser et al., 2017, 2018). Through these circulation changes, tropical Pacific variability influences winter temperature, storm tracks, and precipitation, with potential consequences for snow accumulation, melt timing, and subsequent spring runoff (L'Heureux et al., 2015; Patricola et al., 2020). These connections are particularly relevant to western Canada and the northwestern United States, where winter snow storage plays an important role in seasonal water availability (Fleming & Whitfield, 2010; Whitfield et al., 2010; Bonsal et al., 2017; Dierauer et al., 2019).

Very strong El Niño events are difficult to assess statistically because relatively few independent events have been observed. The amplitude and spatial structure of atmospheric teleconnections can vary nonlinearly with the intensity and distribution of tropical Pacific forcing (Johnson & Kosaka, 2016; Hoell et al., 2016; Takahashi & Dewitte, 2016). In the Niño-3.4 record and event classification adopted here, only three completed events before 2026 reached peak three-month-mean anomalies of at least +2.0 °C: 1982/83, 1997/98, and 2015/16 (Santoso et al., 2017; L'Heureux et al., 2017). Consequently, statistical inference concerning very strong events relies on a limited number of historical analogues. These events have also been studied extensively after their mature-winter circulation and hydroclimatic outcomes became known. Although retrospective analyses are essential for understanding completed events, knowledge of the observed outcomes may influence analogue selection and analytical decisions. Examining a developing event before its winter outcome is known offers a complementary perspective, allowing researchers to document in advance the historical relationships and criteria used for subsequent evaluation.

The developing 2026 El Niño is particularly noteworthy because its rapid tropical Pacific warming has occurred under North Pacific conditions that differ from those accompanying previous very strong events. The PDO reflects variability arising from tropical Pacific forcing through the atmospheric bridge, internal atmospheric processes, and oceanic adjustments (Newman et al., 2016; Zhao et al., 2021; Di Lorenzo et al., 2023; Capotondi et al., 2023). Previous studies have reported differences in ENSO-related climate responses under contrasting PDO conditions. Kim et al. (2014) investigated the combined effects of ENSO and PDO on the East Asian winter monsoon, while Maher et al. (2022) showed that PDO conditions can modulate ENSO-related temperature and precipitation teleconnections over North America. However, covariance between ENSO and PDO, the limited number of high-amplitude events, and the timing used to characterize the PDO state complicate these relationships. Moreover, evidence that the PDO modulates regional temperature and precipitation does not necessarily imply a corresponding change in the relationship between ENSO and the PNA index. Whether a developing-season PDO modifies the subsequent winter Niño-3.4–PNA relationship therefore remains an open question. A

regression model incorporating the Niño-3.4 × PDO interaction tests slope modulation directly; PDO-stratified correlations provide descriptive comparisons.

Very strong El Niño events also differ in their seasonal development. The 1997 event intensified rapidly from relatively cool spring conditions, the 1982 event remained comparatively modest through late summer before strengthening toward winter, and the 2015 event developed from an already warm spring state (Chen et al., 2015; Santoso et al., 2017; L'Heureux et al., 2017). These contrasting trajectories show why mature-winter amplitude alone does not fully describe an El Niño event's evolution. They also raise questions about the use of empirical persistence relationships to estimate winter Niño-3.4 conditions from preceding summer anomalies (Barnston et al., 2019; L'Heureux et al., 2019; Tippett & L'Heureux, 2020). Although such relationships may perform well within the historical record, their predictive performance cannot be assumed to extend beyond the range of values used for calibration. When a developing event exceeds that range, regression estimates become extrapolations with unverified predictive reliability. Establishing the historical predictor domain is therefore necessary when interpreting persistence-based estimates for unusually strong events.

The reliability of these atmospheric relationships also matters for hydrological interpretation. ENSO-related changes in large-scale circulation can alter regional temperature, precipitation, and storm tracks, affecting precipitation phase, snow accumulation, and melt timing in snow-dominated catchments. The resulting streamflow response depends on both meteorological conditions and catchment characteristics, including antecedent moisture, storage, and runoff processes (Fleming & Whitfield, 2010; Whitfield et al., 2010; Dierauer et al., 2019). ENSO-related hydroclimatic signals are generally more pronounced in western Canada and the northwestern United States and less consistent across eastern Canada, where North Atlantic and Arctic circulation variability becomes increasingly important (Tan et al., 2016; Whan & Zwiers, 2017; Nalley et al., 2019). Tropical Pacific influences may also extend into the North Atlantic sector through tropospheric and stratospheric pathways that depend on event characteristics and atmospheric background conditions (Jiménez-Esteve & Domeisen, 2018; Domeisen et al., 2019; Hardiman et al., 2019). Identifying ENSO-related atmospheric relationships helps interpret potential hydroclimatic consequences, but these relationships alone do not establish the magnitude, timing, or spatial distribution of regional hydrological responses.

The developing 2026 El Niño is examined using six climate indices: Niño-3.4, the Southern Oscillation Index (SOI), PDO, PNA, the North Atlantic Oscillation (NAO), and the Arctic Oscillation (AO). The analysis considers the rate of event development, its position within the historical Niño-3.4–PDO distribution, relationships between ENSO and Northern Hemisphere circulation indices, and the persistence of summer Niño-3.4 anomalies into the following winter. The analysis evaluates the statistical evidence for PDO modulation and determines whether the 2026 summer conditions extend beyond the historical predictor range. Based on observations available before winter 2026/27, the study focuses exclusively on climate indices and does not directly assess regional temperature, precipitation, snowpack, or streamflow responses.

This study addresses three objectives. First, it evaluates the exceptional development of the 2026 El Niño by comparing its intensification rate and joint Niño-3.4–PDO configuration with historical observations. Second, it quantifies historical ENSO associations with selected Northern Hemisphere circulation indices and tests whether developing-season PDO modulates the subsequent winter Niño-3.4–PNA relationship. Third, it assesses summer-to-winter ENSO persistence through expanding-window hindcasting and

determines whether the 2026 conditions exceed the historical predictor domain. The proposed framework integrates the assessment of an unusual ENSO–PDO configuration with historical teleconnection and persistence analyses, providing a quantitative benchmark for winter 2026/27 while distinguishing established statistical relationships from their uncertain applicability under exceptional ENSO conditions.

2. Materials and methods

2.1. Prospective diagnostic framework

This study adopts a prospective, observation-constrained diagnostic framework to investigate the exceptional development of tropical Pacific sea-surface temperature (SST) anomalies during 2026 and their potential implications for Northern Hemisphere winter atmospheric circulation. The framework integrates historical event analogs, multivariate climate-state characterization, temporal dependence analysis, and statistical assessment of seasonal persistence. Rather than treating El Niño intensity as an isolated predictor of atmospheric response, the analysis explicitly considers the evolving Pacific background state, the temporal structure of ENSO–circulation relationships, and the limits of historical statistical inference under unusually strong developing conditions. This integrated approach provides a basis for distinguishing observed characteristics of the developing event from historically supported relationships and extrapolations concerning the subsequent winter. The methodological framework comprises four complementary and sequential analytical stages, each addressing a distinct dimension of ENSO evolution and its relationship with large-scale atmospheric variability.

Stage 1: Historical characterization of ENSO development. The first stage quantifies the evolution of Niño-3.4 SST anomalies between March and August 2026 using the absolute anomaly increase and the fitted monthly development slope. These diagnostics are compared with the corresponding historical distributions to assess the event's relative magnitude and rate of development. Comparisons with major historical El Niño episodes further distinguish rapid early-season intensification from mature-event amplitude, avoiding the assumption that exceptional summer development necessarily implies an equally exceptional winter peak (Section 2.4).

Stage 2: Joint characterization of ENSO intensity and the North Pacific background state. The second stage examines the developing event within the historical Niño-3.4–PDO phase space. By jointly evaluating tropical Pacific SST anomalies with the PDO, the analysis moves beyond a univariate description of ENSO intensity to characterize the broader Pacific configuration that accompanies event development. Historical occupancy of the relevant phase-space sector is examined while recognizing the serial dependence of overlapping monthly observations and the distinction between individual observations and independent ENSO events. This stage identifies whether the observed combination of tropical Pacific warming and North Pacific variability is represented within the historical record, without assigning unsupported recurrence probabilities to sparsely sampled climate states (Section 2.5).

Stage 3: ENSO–atmospheric circulation coupling and PDO-dependent relationships. The third stage evaluates the statistical relationships between Niño-3.4 variability and three major Northern Hemisphere

circulation indices: the PNA pattern, NAO, and AO. Monthly lead–lag correlations and winter-targeted seasonal correlations are examined separately to distinguish the temporal organization of climate-index covariability from associations specifically relevant to subsequent winter conditions. Statistical inference uses circular-shift and block-permutation procedures, along with false-discovery-rate adjustment, to account for temporal dependence and multiple comparisons. We evaluate whether the winter Niño-3.4–PNA relationship depends on the developing-season PDO state using a regression interaction term. Additional sensitivity analyses assess the influence of the 1991/92 winter and the robustness of the estimated association to short-range temporal dependence. These analyses provide a structured assessment of statistical coupling and its sensitivity to background conditions, without interpreting correlation or interaction coefficients as evidence of a causal atmospheric mechanism (Section 2.6).

Stage 4: Summer-to-winter ENSO persistence and assessment of historical predictive support. The final stage investigates the historical relationship between June–August (JJA) and subsequent December–February (DJF) Niño-3.4 anomalies. A linear persistence model is evaluated using expanding-window hindcasting, ensuring that each historical prediction is generated without information from its target winter. The observed JJA 2026 anomaly is subsequently assessed relative to the historical predictor domain. The analysis also assesses whether the developing event lies within the historical calibration range, as statistical relationships derived from past observations may not remain reliable when applied to predictor values beyond those previously observed. Regression estimates and associated prediction intervals are therefore interpreted in relation to the degree of extrapolation rather than treated as independently validated forecasts of winter 2026/27 (Section 2.7).

A central methodological consideration is the strict separation between observed event development, historical statistical relationships, and prospective winter inference. The observational cutoff was August 2026. Consequently, only information available by that date was used to characterize the developing event, and no observations from the uncompleted winter of 2026/27 entered the historical winter circulation analyses or persistence-model calibration. Available 2026 observations were retained in descriptive assessments and monthly lead–lag analyses where appropriate. This temporal separation prevents the incorporation of future winter outcomes into the assessment of the developing event and preserves the distinction between retrospective statistical characterization and prospective interpretation. The framework is designed to address three interconnected scientific questions: (i) how unusual the observed 2026 ENSO development and associated Pacific background state are relative to historical conditions; (ii) how tropical Pacific variability is statistically related to subsequent Northern Hemisphere winter circulation, including the potential modifying role of the PDO; and (iii) to what extent historical summer-to-winter ENSO persistence provides a defensible basis for interpreting an event whose developing-season intensity may extend beyond the historical calibration domain. By combining these questions within a consistent temporal framework, the study evaluates both the information provided by historical climate relationships and the limitations of applying those relationships to an unusually strong developing event. Table 1 summarises the six climate-index records, their definitions, temporal resolutions, and observational coverage. Figure 1 illustrates their geographical domains and representative spatial configurations.

Table 1. Inventory of climate-index records used in the analysis, including their definitions, sources, native temporal resolution, and observational coverage.

Figure 1. Geographical overview of six large-scale climate indices: (a) Niño-3.4, SOI, and PDO; (b) PNA, NAO, and AO. Shaded areas and markers indicate representative domains and reference locations.

2.2. Climate-index records

Six climate indices were used to characterize ENSO development, the North Pacific background state, and associated Northern Hemisphere atmospheric circulation: Niño-3.4 SST anomalies, SOI, PDO, PNA, NAO, and AO. These indices provide complementary information on tropical Pacific variability, broader Pacific climate conditions, and atmospheric teleconnections relevant to winter 2026/27. Tropical Pacific SST variability was represented by the Niño-3.4 index, defined as the SST anomaly averaged over 5° S–5° N and 170°–120° W. Weekly anomalies were obtained from the NOAA Optimum Interpolation SST (OISST) product (Reynolds et al., 2002), referenced to the 1991–2020 climatological period. The dataset spans September 1981 to August 2026 and includes 2,348 weekly observations. The atmospheric component of ENSO was characterised using the SOI, calculated from the standardised sea-level-pressure difference between Tahiti and Darwin (Ropelewski & Jones, 1987). Monthly SOI observations were obtained from the NOAA Climate Prediction Center (CPC) for January 1951–July 2026. These two indices represent complementary oceanic and atmospheric aspects of tropical Pacific variability. The North Pacific background state was characterised using the PDO, which describes the dominant spatial pattern of SST variability poleward of 20° N after removal of the global-mean SST anomaly (Mantua et al., 1997; Newman et al., 2016). Monthly PDO values were obtained from the University of Washington/JISAO record distributed through NOAA, covering January 1854–July 2026. The PDO was included to examine whether the unusually strong tropical Pacific warming observed in 2026 coincided with a historically uncommon North Pacific SST configuration and to assess its potential statistical modulation of ENSO–winter circulation relationships.

Northern Hemisphere atmospheric circulation was represented by the PNA, NAO, and AO indices, obtained at monthly resolution from NOAA/CPC for January 1950–August 2026. The PNA and NAO indices are derived from rotated principal-component analysis of 500-hPa geopotential-height anomalies over 20°–90° N (Barnston & Livezey, 1987), whereas the AO is based on the leading empirical orthogonal function of 1000-hPa geopotential-height anomalies poleward of 20° N. The PNA was used to assess PNA circulation variability associated with ENSO, while the NAO and AO provided complementary diagnostics of North Atlantic and hemispheric-scale circulation relationships. All analyses used the available observational records without additional detrending or standardisation. Because the indices differ in their physical definitions, reference periods, and normalisation procedures, their absolute magnitudes were not compared directly. Statistical analyses were restricted to temporally aligned observations, with missing values excluded from the corresponding calculations. Observations from 2026 were treated as preliminary at the August 2026 cutoff. Table 1 summarises the data sources,

native temporal resolutions, and observational coverage, while Table S1 provides additional information on data provenance, reference periods, and sample sizes.

2.3. Temporal processing, event classification and reference sample

The weekly Niño-3.4 record was linearly interpolated to daily resolution and subsequently aggregated into calendar-month means, yielding 540 monthly anomalies from September 1981 to August 2026, denoted by N_t. To characterize sustained tropical Pacific warming and reduce short-term variability, a centered three-month running mean was calculated as:

$$N_t^{(3)} = \frac{N_{t-1} + N_t + N_{t+1}}{3} \quad (1)$$

where N_t represents the monthly Niño-3.4 anomaly at month t, and N_{t-1} and N_{t+1} denote the preceding and following monthly anomalies, respectively. The resulting series covers October 1981–July 2026. Although this smoothing procedure captures persistent SST anomalies, it differs from the operational Oceanic Niño Index (ONI) in its underlying SST product and climatological reference procedure. Consequently, the classifications derived here are not directly interchangeable with operational ONI classifications. Seasonal indices were calculated as the arithmetic mean of three consecutive monthly observations. JJA and SON were assigned to their calendar years, whereas DJF was labeled according to the January year. For example, DJF 1998 comprises December 1997–February 1998 and represents the mature winter associated with the 1997 developing event. At the August 2026 observational cutoff, the monthly Niño-3.4 anomaly reached +2.55 °C, while the latest available centered three-month mean, corresponding to JJA 2026, was +2.12 °C.

ENSO episode identification and seasonal amplitude classification were treated as distinct procedures. The conventional duration criterion requires at least five consecutive overlapping three-month periods with Niño-3.4 anomalies of +0.5 °C or greater to identify a sustained warm episode. Separately, DJF Niño-3.4 anomalies were classified into six study-defined magnitude categories: cold (≤−0.5 °C), neutral (−0.5 to less than +0.5 °C), weak warm (+0.5 to less than +1.0 °C), moderate warm (+1.0 to less than +1.5 °C), strong warm (+1.5 to less than +2.0 °C), and very strong warm (≥+2.0 °C). These categories were used exclusively to compare winter circulation conditions across different SST anomaly magnitudes and were not interpreted as independent ENSO episode classifications. Historical event comparisons focused on the completed high-amplitude El Niño episodes of 1982/83, 1997/98, and 2015/16, selected to evaluate differences in seasonal development among major historical events. The 1991/92 episode was additionally retained as a reference and sensitivity case because of its proximity to the June 1991 Mount Pinatubo eruption. Table 2 presents the selected developing years and their analytical roles.

Table 2. Historical reference years and the developing 2026 event considered in the analysis.

The 2026 event was evaluated strictly using observations available through August 2026. Although the JJA Niño-3.4 mean exceeded +2.0 °C, only four consecutive overlapping three-month periods met the +0.5 °C threshold. Thus, the five-period duration criterion had not yet been fulfilled, and the eventual duration, peak amplitude, and mature-winter conditions remained undetermined. Accordingly, 2026 was excluded from all historical winter composites and regression calibrations requiring observations from DJF 2026/27. Analysis-specific reference samples were defined according to data availability and temporal alignment. March–August development was evaluated over 45 years (1982–2026), with the 2026 trajectory compared against 44 preceding years. Winter circulation analyses covered 45 completed DJF seasons (1982–2026). Associations between developing-season JJA Niño-3.4 and subsequent winter circulation used 44 paired observations, whereas SON and concurrent DJF associations included 45 observations. Summer-to-winter persistence was evaluated using 44 developing years (1982–2025). Joint Niño-3.4–PDO analyses were restricted to their common observational period, with centered three-month Niño-3.4 values available from October 1981 to July 2026. Detailed sample definitions are provided in Table S2. This analysis-specific temporal alignment preserves the distinction between the observed development of the 2026 event and historical relationships used to assess subsequent winter conditions. Available 2026 observations were included in event-development diagnostics, the Niño-3.4–PDO phase-space analysis, and monthly lead–lag correlations where applicable, but no unobserved winter 2026/27 information entered the historical winter analyses or persistence-model calibration.

2.4. Characterization of March–August Niño-3.4 development

The rate and magnitude of ENSO development were quantified using monthly Niño-3.4 anomalies from March to August for each year during 1982–2026. This fixed six-month window captures the transition from boreal spring to late summer and provides a consistent basis for comparing the developing 2026 event with historical tropical Pacific SST evolution. Two complementary diagnostics were employed: the net anomaly increase and the linear development slope. The net March–August change was calculated as:

$$\Delta N_y = N_{y,\mathrm{Aug}} - N_{y,\mathrm{Mar}}. \quad (2)$$

where ΔN_y is the Niño-3.4 anomaly change (°C) in year y, and $N_{y,\mathrm{Aug}}$ and $N_{y,\mathrm{Mar}}$ are the corresponding August and March monthly anomalies, respectively. Positive values indicate net warming over the development period, whereas negative values indicate cooling. The relative magnitude of the 2026 increase was evaluated against the 44 preceding years (1982–2025) using a descending empirical rank

$$R_{2026} = 1 + \sum_{k \neq 2026} I\left(\Delta N_k > \Delta N_{2026}\right) \quad (3)$$

where R_{2026} denotes the rank of the 2026 anomaly increase, k indexes the historical comparison years, and $I(\cdot)$ is an indicator function equal to one when the specified condition is satisfied and zero otherwise. A rank of one indicates that the 2026 increase exceeds or equals all historical values in the available

record. This ranking provides an empirical measure of historical extremeness but does not establish a recurrence interval or exceedance probability.

To complement the endpoint-based measure, an ordinary least-squares linear trend was fitted to the six-monthly Niño-3.4 anomalies from March through August of each year. The resulting slope (°C month^{-1}) characterizes the average rate of SST anomaly development across the full interval, reducing reliance on the two endpoint observations alone. The net change and fitted slope therefore describe distinct aspects of event evolution: cumulative intensification and the average monthly development rate, respectively. Both diagnostics were applied to the historical record and the developing 2026 event, with comparisons focusing on the 1982, 1991, 1997, and 2015 reference years. These comparisons quantify differences in ENSO development trajectories and intensification rates without assuming that rapid spring-to-summer warming leads to greater winter intensity. Neither diagnostic was used in the summer-to-winter persistence model, preserving the distinction between historical event characterization and winter inference. The development trajectories, estimated slopes, and empirical rankings are presented in Section 3.2.

2.5. Historical Niño-3.4–PDO phase space

The Pacific background conditions accompanying ENSO development were examined through the joint distribution of Niño-3.4 and PDO anomalies. This bivariate approach characterises the evolving tropical Pacific SST state in relation to North Pacific variability, allowing the 2026 event to be assessed beyond its Niño-3.4 amplitude alone. The analysis used the centred three-month Niño-3.4 mean and concurrent monthly PDO observations over their common period, October 1981–July 2026. The overall statistical association between the two indices was quantified using Pearson's correlation coefficient. Their joint variability was further examined in the Niño-3.4–PDO phase space, with emphasis on the combination of pronounced tropical Pacific warming and negative PDO conditions observed during 2026. The July 2026 state was evaluated against the historical sector defined by a three-month Niño-3.4 anomaly greater than +2.0 °C and a PDO index below −1.5, denoted by Ω_{2026}. Historical occupancy of this sector was assessed using paired monthly observations preceding 2026 to determine whether comparable combinations had occurred within the available record. Because consecutive three-month Niño-3.4 means overlap and both indices exhibit temporal persistence, individual monthly observations were not considered statistically independent realizations of ENSO–PDO conditions. Accordingly, phase-space occupancy was interpreted as a descriptive measure of historical representation rather than an estimate of event frequency, recurrence probability, or return period. The thresholds defining Ω_{2026} were selected to characterize the observed 2026 configuration and were not treated as independently established thresholds of climatic extremeness. Similarly, the correlation between Niño-3.4 and PDO was interpreted as evidence of statistical covariability rather than causal coupling.

To characterize the PDO background state during ENSO development, monthly PDO anomalies were additionally averaged over March–July for each developing year. This fixed pre-winter window provides a consistent seasonal descriptor of North Pacific conditions and was retained for the PDO-stratified comparisons and interaction analysis of the subsequent winter Niño-3.4–PNA relationship (Section 2.6). Using the same PDO aggregation across these analyses ensures consistency between the phase-space characterization and the assessment of potential background-state modulation of winter circulation.

2.6. ENSO–circulation relationships and PDO modulation

The relationships between tropical Pacific variability and Northern Hemisphere atmospheric circulation were investigated using the PNA, NAO, and AO indices. The analysis was designed to distinguish monthly lead–lag covariability from seasonally resolved associations with winter circulation and to determine whether the developing-season PDO state modifies the Niño-3.4–PNA relationship. A complementary statistical framework combining correlation analysis, dependence-aware inference, regression interaction modelling, and sensitivity testing was employed to evaluate the strength, temporal structure, and robustness of these relationships.

2.6.1. Monthly and seasonal correlations

Monthly lead–lag correlations were calculated to describe the temporal relationships between Niño-3.4 variability and the three atmospheric circulation indices. To represent sustained tropical Pacific conditions while avoiding the inclusion of future observations in the predictor, a trailing three-month Niño-3.4 mean was constructed from the current and two preceding monthly anomalies. Pearson correlations were then evaluated over lags ranging from −6 to +6 months:

$$r_C(\ell) = \mathrm{corr}\left(N_t^{(3,\mathrm{tr})}, C_{t+\ell}\right), \qquad \ell = -6, \ldots, +6, \tag{4}$$

where $r_C(l)$ is the correlation coefficient at lag l, $N_t^{(3,\mathrm{tr})}$ denotes the trailing three-month Niño-3.4 mean ending in month t, and C_{t+l} represents the PNA, NAO, or AO index at the corresponding lag. Positive lags indicate that the circulation index follows Niño-3.4, whereas negative lags indicate that circulation variations precede the SST anomalies. The lag structure was interpreted as a diagnostic of temporal association rather than evidence of directional causality.

Because monthly correlations may reflect relationships that differ from those governing winter circulation, a separate seasonal analysis was conducted. Developing-season JJA and SON Niño-3.4 anomalies were related to the subsequent DJF circulation indices, while concurrent DJF correlations were calculated to assess wintertime associations:

$$\begin{gathered} r_C^S = \mathrm{corr}\left(N_{y-1}^S, C_y^{\mathrm{DJF}}\right), \quad S \in \{\mathrm{JJA,SON}\}, \\ r_C^{\mathrm{DJF}} = \mathrm{corr}\left(N_y^{\mathrm{DJF}}, C_y^{\mathrm{DJF}}\right). \end{gathered} \tag{5}$$

here, N_{y-1}^S denotes the developing-season Niño-3.4 mean preceding winter y, N_y^{DJF} is the concurrent winter Niño-3.4 mean, and C_y^{DJF} represents the corresponding winter circulation index. The JJA analysis comprised 44 paired observations, whereas SON and concurrent DJF analyses included 45 completed winters. This separation between developing-season and concurrent winter relationships is important for interpretation. JJA and SON correlations describe the historical association between antecedent tropical Pacific conditions and subsequent winter circulation, whereas DJF correlations quantify contemporaneous covariability. Accordingly, concurrent winter relationships were not interpreted as evidence of predictive skill from preceding seasons.

2.6.2. Inference and multiple comparisons

Statistical inference was designed to account for temporal dependence in the climate-index records and the multiplicity of correlation tests. Conventional correlation significance tests based on independent observations may underestimate uncertainty when climate indices exhibit serial persistence. Resampling procedures that retain aspects of the observed temporal structure were therefore used. For the seasonal correlations, statistical significance was evaluated using two-sided block permutations of the atmospheric circulation series relative to Niño-3.4. The procedure employed three-year blocks, random circular offsets, and 20,000 permutations to accommodate short-range temporal dependence while disrupting the original cross-series alignment. The empirical probability was estimated as

$$p = \frac{1 + \sum_{b=1}^{B} I\left(\left|r_b^{\mathrm{perm}}\right| \geq |r|\right)}{B + 1}, \qquad B = 20{,}000, \tag{6}$$

where r is the observed correlation coefficient, r_b^{perm} is the coefficient obtained from permutation b, B is the number of permutations, and $I(\cdot)$ is the indicator function. The two-sided formulation evaluates departures from the null distribution in either direction without imposing an expected sign on the ENSO–circulation relationship. For monthly lead–lag correlations, significance was assessed by circularly shifting the atmospheric-index series relative to Niño-3.4. This procedure preserves the internal temporal ordering of each series while modifying their relative alignment. Because circular shifting does not eliminate all potential effects of low-frequency variability or nonstationarity, the resulting probabilities were interpreted as dependence-aware measures of statistical evidence rather than definitive tests of physical coupling.

To limit false discoveries across the multiple correlation tests, the Benjamini–Hochberg procedure was applied separately to the nine seasonal correlations and 39 monthly lag correlations, using a false-discovery-rate threshold of 0.05 (Benjamini & Hochberg, 1995; Wilks, 2016). The two test families were treated separately because they address different temporal questions and have different sampling structures. Seasonal correlations were prioritized for interpreting relationships relevant to winter circulation, while monthly correlations provided complementary information on temporal covariability.

2.6.3. ENSO-amplitude and PDO-stratified comparisons

To test whether winter circulation characteristics vary with ENSO amplitude, we grouped DJF PNA, NAO, and AO values by the Niño-3.4 magnitude categories defined in Section 2.3. Within each category, the mean and standard deviation of the circulation indices were calculated to describe differences in their central tendency and dispersion across cold, neutral, and progressively warmer tropical Pacific conditions. Individual high-amplitude historical events were additionally examined to assess the consistency of circulation responses under strong tropical Pacific warming. Given the limited number of completed very strong El Niño winters, these comparisons were considered descriptive and were not used to establish a generalised circulation response for extreme ENSO conditions. The potential influence of the North Pacific background state was initially explored by stratifying the winter Niño-3.4–PNA relationship according to the sign of the developing-season March–July PDO mean. Separate correlations and linear regression slopes were calculated for positive and non-positive PDO conditions. This stratification provides an interpretable comparison of ENSO–PNA associations under contrasting PDO states, although differences between subgroup estimates may arise from sampling variability, unequal sample sizes, or

differences in the distribution of Niño-3.4 anomalies. Consequently, the stratified results were treated as exploratory diagnostics. Formal statistical evidence for PDO-dependent variation in the Niño-3.4–PNA relationship was evaluated using the interaction model described below.

2.6.4. Interaction model for PDO modulation

The potential modulation of the winter Niño-3.4–PNA relationship by developing-season PDO was evaluated using a multiple linear regression model incorporating the interaction between winter Niño-3.4 and antecedent PDO conditions:

$$\mathrm{PNA}_y^{\mathrm{DJF}} = \beta_0 + \beta_1 N_{c,y}^{\mathrm{DJF}} + \beta_2 P_{c,y} + \beta_3 \left(N_{c,y}^{\mathrm{DJF}} P_{c,y}\right) + \varepsilon_y, \quad (7)$$

where $\mathrm{PNA}_y^{\mathrm{DJF}}$ is the winter PNA index in year y, $N_{c,y}^{\mathrm{DJF}}$ is the mean-centred winter Niño-3.4 anomaly, and $P_{c,y}$ is the mean-centred March–July PDO index from the preceding developing year. The coefficients β_0, β_1, and β_2 represent the intercept and the conditional main effects of Niño-3.4 and PDO, respectively, while β_3 quantifies their statistical interaction. The residual term ε_y represents variability not explained by the model.

Both predictors were centered before constructing the interaction term. Under this parameterization, β_1 represents the winter Niño-3.4–PNA regression slope at the mean developing-season PDO state, while β_2 represents the PDO association at the mean winter Niño-3.4 anomaly. The interaction coefficient β_3 describes the change in the conditional Niño-3.4–PNA slope per unit increase in PDO. The null hypothesis $\beta_3 = 0$ was used to test whether the linear association between winter Niño-3.4 and PNA varies systematically with the antecedent PDO state. The model was estimated by ordinary least squares using 45 completed winters. To account for potential heteroskedasticity and short-range serial dependence in the annual residuals, coefficient uncertainty was evaluated using the Newey–West heteroskedasticity- and autocorrelation-consistent covariance estimator with a truncation lag of three years (Newey & West, 1987, 1994). Two-sided probabilities were calculated for the estimated coefficients.

The interaction analysis provides a formal statistical assessment of whether the historical ENSO–PNA association is conditional on the developing-season PDO state. However, because winter Niño-3.4 and PNA are contemporaneous variables, the fitted interaction represents conditional winter covariability rather than a prospective prediction model based exclusively on antecedent information. Furthermore, a statistically significant interaction would establish variation in the observed regression relationship, not a causal mechanism through which PDO modifies the atmospheric response to ENSO.

2.6.5. Sensitivity of the winter Niño-3.4–PNA association

The robustness of the winter Niño-3.4–PNA association was assessed through complementary event-exclusion and block-bootstrap analyses. These tests were designed to evaluate whether the estimated relationship depends strongly on an individual historically unusual winter or on assumptions concerning the effective independence of annual observations. First, the winter Niño-3.4–PNA correlation was recalculated after excluding DJF 1991/92, which followed the June 1991 Mount Pinatubo eruption

(Khodri et al., 2017). Comparing the full-sample and reduced-sample correlations provides a targeted assessment of the sensitivity of the estimated ENSO–PNA association to this potentially influential period. This exclusion was not intended to isolate or quantify the volcanic contribution to atmospheric circulation. Sampling uncertainty was further assessed using a circular moving-block bootstrap of paired annual Niño-3.4 and PNA observations (Künsch, 1989). Joint resampling preserved the contemporaneous pairing of the indices, while consecutive-year blocks accounted for short-range temporal dependence. Block lengths of two to five years were tested, with 10,000 bootstrap replicates for each block length and sample configuration. Percentile-based 95% confidence intervals were calculated for the Pearson correlation coefficient. The bootstrap analysis was performed for both the complete winter sample and the sample excluding DJF 1991/92. Examining multiple block lengths allows us to assess how sensitive the estimated uncertainty is to the assumed dependence horizon, without relying on a single block specification. The resulting intervals were interpreted as measures of sampling uncertainty conditional on the observed record and the resampling procedure. The event-exclusion and block-bootstrap analyses confirm the robustness of the historical winter Niño-3.4–PNA correlation to the tested specifications. However, the limited sample size and the exceptional magnitude of the developing 2026 event introduce uncertainty about whether this relationship applies beyond the historical range. These robustness checks also do not establish significant PDO modulation of the association.

2.7. Summer-to-winter persistence and predictor-domain assessment

Summer-to-winter persistence of tropical Pacific SST anomalies was examined to assess the statistical relationship between developing-season ENSO conditions and subsequent winter intensity. The analysis distinguishes historical predictive skill from the uncertainty associated with extrapolation beyond the calibration range, particularly given the exceptional 2026 summer Niño-3.4 anomaly. The historical relationship between JJA and subsequent DJF Niño-3.4 anomalies was represented using a linear regression model:

$$N_{y+1}^{\mathrm{DJF}} = \alpha + \beta N_{y}^{\mathrm{JJA}} + \varepsilon_y \tag{8}$$

where N_y^{JJA} is the summer Niño-3.4 anomaly in the developing year y, N_{y+1}^{DJF} is the corresponding subsequent winter anomaly, α and β are the regression intercept and slope, respectively, and ε_y is the residual error. The model was calibrated using 44 completed developing-year–winter pairs from 1982–2025. The 2026 event was excluded because its subsequent winter conditions were unavailable at the observational cutoff. To evaluate predictive performance under a temporally consistent validation scheme, an expanding-window hindcasting procedure was implemented. The initial calibration period comprised developing years 1982–1996, and the model was subsequently refitted as each additional historical year became available. At each iteration, the following winter anomaly was estimated using only preceding developing-year–winter pairs, thereby preventing future winter information from entering the corresponding model calibration. This procedure generated 29 out-of-sample hindcasts for developing years 1997–2025. Hindcast performance was quantified using the out-of-sample coefficient of determination

$$R_{\mathrm{EW}}^2 = 1 - \frac{\sum_{i\in H}(y_i - \hat{y}_i)^2}{\sum_{i\in H}(y_i - \bar{y}_H)^2} \tag{9}$$

where H denotes the set of hindcast years, y_i and $\hat{y}_i$ are the observed and out-of-sample estimated DJF Niño-3.4 anomalies, respectively, and $\bar{y}_H$ is the mean observed anomaly over the hindcast evaluation period. Positive values indicate improvement over the retrospective mean benchmark, whereas negative values indicate that the accumulated hindcast errors exceed those of this benchmark. Because the denominator uses the mean of the complete evaluation period, R^2_{EW} was interpreted as a retrospective skill diagnostic rather than a comparison against a strictly prospective climatological forecast. Following hindcast evaluation, the regression was refitted using all 44 historical pairs and evaluated at the observed JJA 2026 anomaly. Under the conventional linear-regression assumptions, the 95% prediction interval for an individual subsequent winter anomaly was calculated as

$$\hat{y}_0 \pm t_{0.975,n-2}\, s \sqrt{1 + \frac{1}{n} + \frac{(x_0 - \bar{x})^2}{S_{xx}}}, \tag{10}$$

where $\hat{y}_0$ is the fitted DJF Niño-3.4 anomaly corresponding to the 2026 summer predictor x_0, $t_{0.975,n-2}$ is the 97.5th percentile of the Student's t-distribution with $n-2$ degrees of freedom, $n = 44$ is the calibration sample size, s is the residual standard deviation, $\bar{x}$ is the historical mean JJA anomaly, and S_{xx} is the sum of squared deviations of the historical JJA anomalies from $\bar{x}$. The interval incorporates residual variability and uncertainty in the estimated conditional mean under the assumed linear model. The applicability of this regression to the 2026 event was assessed by explicitly examining the position of its summer anomaly relative to the historical calibration domain, defined by the minimum and maximum JJA Niño-3.4 anomalies, $[x_{\min}, x_{\max}]$. For a predictor exceeding the historical maximum, the relative extent of extrapolation was quantified as

$$\delta = \frac{x_0 - x_{\max}}{x_{\max} - x_{\min}}. \tag{11}$$

where δ represents the exceedance above the historical maximum normalised by the observed calibration range. A positive value indicates that the 2026 summer anomaly lies outside the historical predictor domain, with larger values corresponding to greater relative extrapolation. This diagnostic measures distance beyond the sampled range but does not quantify the event's probability or establish the reliability of the extrapolated regression relationship. The distinction between interpolation and extrapolation is central to interpreting the persistence analysis. Expanding-window hindcasting evaluates model performance under historical ENSO conditions but does not establish predictive reliability for summer anomalies beyond those represented in the calibration record. Furthermore, the conventional prediction interval assumes that the fitted linear relationship, residual variance, and underlying error structure remain applicable at the evaluated predictor value. These assumptions cannot be independently verified for an unprecedented summer anomaly. Accordingly, the regression estimate and prediction interval evaluated at JJA 2026 were treated as conditional extrapolation diagnostics rather than a calibrated probabilistic forecast of DJF 2026/27. This approach retains the information contained in historical ENSO persistence while explicitly recognizing the limits of statistical transferability to unusually strong developing conditions. The historical regression, expanding-window hindcast performance, and position of the 2026 predictor relative to the calibration domain are presented in Section 3.5.

3. Results

3.1. Tropical Pacific ocean–atmosphere state through August 2026

The historical Niño-3.4 record exhibits pronounced interannual variability, with major warm and cold episodes clearly represented in the centered three-month series (Figure 2a). Three completed El Niño events reached peak three-month anomalies of at least +2.0 °C: 1982/83, 1997/98, and 2015/16, whereas the 2023/24 event peaked at approximately +1.91 °C. During 2026, tropical Pacific warming intensified substantially, with the monthly Niño-3.4 anomaly reaching +2.55 °C in August. The corresponding JJA mean was +2.12 °C, representing the latest available centred three-month value at the observational cutoff. Although this magnitude indicates exceptionally strong developing-season SST anomalies, the five-period duration criterion defined in Section 2.3 had not yet been satisfied. Consequently, the observed warming was characterised as an exceptionally strong developing event rather than a confirmed sustained El Niño episode, and its eventual peak intensity and winter evolution remained undetermined.

The atmospheric component of tropical Pacific variability exhibited a concurrent negative SOI anomaly (Figure 2b). The July 2026 SOI reached −4.0, consistent with the negative SOI conditions generally associated with tropical Pacific warming. The simultaneous occurrence of strongly positive Niño-3.4 and negative SOI anomalies is consistent with the ocean–atmosphere coupling characteristic of El Niño development. However, the available observations do not establish the subsequent persistence or mature-winter atmospheric response. The recent evolution of all six climate indices from January 2024 through their respective observational cutoffs is presented in Figure S1.

Figure 2. Historical evolution of tropical Pacific oceanic and atmospheric indices through August 2026. (a) Weekly Niño-3.4 anomalies (grey), centred three-month means (black), and positive and negative anomaly shading (red and blue, respectively). Labelled winters are those whose DJF-mean Niño-3.4 anomaly reached +2.0 °C (1982/83 and 2015/16); the 1997/98 event, whose peak three-month mean exceeded +2.0 °C but whose DJF mean was +1.98 °C, is not labelled. (b) Monthly SOI, with positive and negative values distinguished by blue and red shading. Orange stars indicate the latest available monthly observations: August 2026 for Niño-3.4 (+2.55 °C) and July 2026 for SOI (−4.0). The latest available centred Niño-3.4 mean corresponds to JJA 2026 (+2.12 °C).

3.2. March–August development of the 2026 event

The 2026 Niño-3.4 evolution exhibited an exceptionally rapid transition from weak negative anomalies in early winter to pronounced tropical Pacific warming by late summer (Figure 3a). The monthly anomaly increased from −0.58 °C in January to +0.04 °C in March, reaching +2.55 °C in August. This August value exceeded the corresponding anomalies of the three completed very strong historical reference events: 1997 (+1.76 °C), 2015 (+1.67 °C), and 1982 (+0.81 °C). Relative to 1997, which exhibited the highest August anomaly among these reference events, the 2026 value was 0.79 °C greater. The historical trajectories also reveal distinct development patterns, including substantial intensification after August 1982 and comparatively elevated SST anomalies during spring 2015. These differences indicate that similar mature-event intensities can emerge from substantially different seasonal development trajectories. The March–August Niño-3.4 increase in 2026 reached +2.52 °C, ranking first among the 45 years examined during 1982–2026 (Figure 3b; Table 3). This increase exceeded the second-largest

historical change, recorded in 1997 (+2.10 °C), by approximately 0.41 °C. The fitted six-month development slope also reached its maximum observed value in 2026 (+0.510 °C month^{-1}), compared with +0.428 °C month^{-1} in 1997, +0.214 °C month^{-1} in 2015, and +0.157 °C month^{-1} in 1982. The agreement between the endpoint-based increase and the fitted slope confirms that the exceptional 2026 development was evident in both the net warming and its average monthly rate, rather than being identified solely from the August anomaly. Despite this unprecedented spring–summer intensification in the available record, historical reference events show that developing-season warming rates do not uniquely determine subsequent winter intensity. In particular, the 1982 event warmed substantially after August, whereas the 2015 event developed from relatively warm spring conditions. The 2026 rankings therefore establish the exceptional magnitude and rate of the observed March–August development, without implying a corresponding ranking of eventual winter intensity. The relationship between summer anomalies and subsequent winter conditions is examined separately through the historical persistence analysis in Section 3.5.

Figure 3. March–August Niño-3.4 development in 2026 relative to selected historical El Niño events. (a) Monthly Niño-3.4 anomalies for developing years 1982, 1991, 1997, 2015, and 2026. The shaded interval identifies March–August, used to quantify event development. Historical trajectories extend through the following March, whereas the 2026 record ends in August. (b) March–August Niño-3.4 anomaly changes for 1982–2026 (45 years), with selected reference years highlighted. The annotation identifies the 2026 empirical rank, net anomaly increase, and fitted six-month development slope.

Table 3. March–August Niño-3.4 development metrics and March–July PDO background conditions for selected historical El Niño events and the developing 2026 event.

3.3. North Pacific background state and Niño-3.4–PDO covariability

The 2026 ENSO developed under persistently negative PDO conditions, contrasting with the predominantly positive North Pacific background states that accompanied several historical high-amplitude El Niño events (Figure 4a). The PDO reached −3.59 in July 2025 and remained negative through July 2026, when it was −1.73. The March–July 2026 mean was −1.53 (Table 3), compared with +1.44 in 1997, +0.86 in 2015, and −0.16 in 1982. Thus, among the three completed very strong reference events, none showed a developing-season PDO as negative as the one observed in 2026. This contrast indicates that the exceptional tropical Pacific warming documented in Section 3.2 developed against a substantially different North Pacific background state than that accompanying the strongest historical reference events. Across the 538 paired monthly observations from October 1981 to July 2026, the centred three-month Niño-3.4 anomaly and concurrent PDO exhibited a weak positive correlation ($r = 0.27$; Figure 4b). Despite this overall positive covariability, the July 2026 state combined a Niño-3.4 anomaly of +2.12 °C with a PDO index of −1.73, placing it within the high-amplitude, negative-PDO sector Ω_{2026} defined in Section 2.5. None of the 531 paired monthly observations preceding 2026 simultaneously satisfied the criteria of Niño-3.4 greater than +2.0 °C and PDO below −1.5. Historical observations exceeding the +2.0 °C Niño-3.4 threshold were associated with the 1982/83, 1997/98, and

2015/16 events, all of which exhibited higher concurrent PDO values. The absence of historical observations within Ω_{2026} indicates that the July 2026 configuration was not represented in the preceding observational record. However, because consecutive monthly observations are temporally dependent and the sector thresholds characterize the observed 2026 state, this finding does not provide an estimate of recurrence probability or statistical significance. The result instead identifies a historically unrepresented combination of tropical Pacific warming and North Pacific SST variability. Whether the developing-season PDO state is associated with systematic differences in subsequent winter circulation is examined through the stratified and interaction analyses in Section 3.4.

Figure 4. North Pacific background variability and historical Niño-3.4–PDO phase space. (a) Monthly PDO from 1950 to July 2026 and its centered 25-month running mean. The orange star indicates July 2026 (PDO = −1.73). (b) Joint distribution of concurrent monthly PDO and centred three-month Niño-3.4 anomalies for October 1981–July 2026 ($n = 538$; Pearson $r = 0.27$). Historical reference Julys are identified in grey, while the orange trajectory represents January–July 2026, terminating at Niño-3.4 = +2.12 °C and PDO = −1.73. The high-amplitude, negative-PDO sector Ω_{2026} is defined by Niño-3.4 greater than +2.0 °C and PDO below −1.5. No paired monthly observation before 2026 fell into this sector.

3.4. Seasonal ENSO–circulation relationships and PDO modulation

3.4.1. Monthly and seasonal ENSO–circulation associations

The monthly lead–lag analysis revealed distinct relationships between Niño-3.4 variability and the three Northern Hemisphere circulation indices (Figure 5a; Figure S2). The PNA showed the strongest association, with correlations increasing from -0.08 at a lag of -6 months to about +0.22 when the PNA followed Niño-3.4 by two to three months. Both positive-lag correlations remained statistically significant after circular-shift inference and false-discovery-rate adjustment across the 39 monthly tests ($q = 0.036$). No other lag–index combination satisfied the adjusted significance threshold. In contrast, correlations involving NAO and AO remained weak across the examined lags, with absolute coefficients not exceeding 0.07 and 0.11, respectively. These results indicate a detectable lagged association between tropical Pacific SST variability and PNA, whereas comparable monthly relationships were not identified for NAO or AO. Seasonal analysis revealed substantially stronger Niño-3.4–PNA associations when circulation was evaluated specifically during DJF (Figure 5b; Table S3). The correlation between developing-year JJA Niño-3.4 and subsequent winter PNA was $r = 0.55$ ($n = 44$), increasing to $r = 0.59$ for SON ($n = 45$). The concurrent DJF relationship was similarly positive ($r = 0.56$, $n = 45$; Figure S3). All three associations remained significant under three-year block-permutation inference with adjustment across the nine seasonal comparisons ($q \approx 0.001$). By comparison, the corresponding NAO correlations ranged from +0.04 to +0.06, while AO correlations ranged from -0.17 to -0.08; none reached statistical significance. The contrast between monthly and winter-targeted correlations indicates that the Niño-3.4–PNA relationship is more clearly expressed when the analysis is conditioned on the winter season. Importantly, the positive JJA and SON correlations establish historical associations between antecedent ENSO conditions and subsequent winter PNA, whereas the concurrent DJF correlation describes wintertime covariability. These relationships are statistically distinct and should not be interpreted as equivalent measures of predictive performance.

3.4.2. Winter circulation across ENSO-amplitude classes

The distribution of winter circulation indices across the Niño-3.4 magnitude classes revealed a consistent positive mean PNA during warm conditions (Table 4; Figure S4). The neutral category exhibited a mean PNA of −0.05, compared with +0.78 for weak-warm winters, +0.72 for moderate-warm winters, +0.73 for strong-warm winters, and +1.25 for very strong-warm winters. The cold category had a mean PNA of +0.15. Although the highest mean occurred in the very strong-warm category, this class contained only two winters, while the moderate-warm category contained a single observation. Consequently, these differences describe the observed distribution of winter circulation rather than a statistically established monotonic response to increasing ENSO amplitude. The three completed historical events classified as very strong according to their peak three-month Niño-3.4 anomalies, 1982/83, 1997/98, and 2015/16, exhibited positive DJF PNA values of +1.08, +0.93, and +1.43, respectively (Table 5). Their corresponding NAO and AO indices differed in both magnitude and sign, indicating that similar high-amplitude ENSO conditions were not accompanied by uniform responses across the three circulation indices. The events also developed under contrasting March–July PDO conditions, ranging from -0.16 in 1982 to +1.44 in 1997 and +0.86 in 2015. These event-level differences motivate examination of whether the antecedent PDO state systematically modifies the winter Niño-3.4–PNA association.

3.4.3. PDO-stratified relationships and interaction analysis

Stratification by the sign of the preceding March–July PDO showed positive winter Niño-3.4–PNA correlations under both conditions (Figure 5c), with r = 0.62 for positive PDO and r = 0.51 for non-positive PDO. Although the correlation was slightly stronger under positive PDO conditions, this descriptive difference does not establish significant PDO modulation, particularly given the limited sample sizes and potentially different Niño-3.4 distributions across the two groups. The formal interaction model (Eq. 7) provided no statistically significant evidence that developing-season PDO modified the winter Niño-3.4–PNA regression slope (Table 6; Figure S5). The estimated interaction coefficient was $\beta_3 = +0.0488$, with a HAC standard error of 0.0353 and $p = 0.174$. The conditional Niño-3.4 coefficient at the mean PDO state was positive and statistically significant ($\beta_1 = +0.2984$, $p < 0.001$), whereas the PDO main effect was negligible ($\beta_2 = -0.0038$, $p = 0.949$). Thus, the positive winter Niño-3.4–PNA association remained evident after accounting for antecedent PDO and its interaction, but the available 45-winter sample did not provide sufficient statistical evidence for a PDO-dependent change in its slope. These findings distinguish the historically unusual joint Niño-3.4–PDO configuration observed in 2026 (Section 3.3) from the statistical evidence required to establish PDO modulation of winter circulation. Although the 2026 event developed under markedly negative PDO conditions, the interaction results do not support a conclusion that this background state necessarily weakens or strengthens the subsequent ENSO–PNA association. The analysis therefore identifies a robust positive historical Niño-3.4–PNA relationship, while leaving the proposed PDO-dependent modulation statistically unresolved.

Figure 5. Monthly and seasonal Niño-3.4 relationships with Northern Hemisphere atmospheric circulation and developing-season PDO. (a) Pearson correlations between the trailing three-month Niño-3.4 mean and PNA, NAO, and AO at lags from −6 to +6 months. Positive lags indicate that atmospheric circulation follows Niño-3.4; open symbols identify correlations significant after circular-shift inference and false-discovery-rate adjustment ($q < 0.05$). (b) Correlations between developing-year JJA ($n = 44$), SON ($n = 45$), and concurrent DJF ($n = 45$) Niño-3.4 anomalies and winter circulation indices. (c) Winter Niño-3.4–PNA relationships stratified by the sign of preceding March–July PDO, with subgroup correlations and the HAC interaction-test probability indicated.

Table 4. DJF PNA, NAO, and AO statistics across study-defined winter Niño-3.4 magnitude classes for 45 completed winters (1982–2026).

Table 5. DJF Niño-3.4 and atmospheric circulation indices for the three completed historical El Niño events with peak three-month Niño-3.4 anomalies of at least +2.0 °C.

Table 6. Regression coefficients and HAC inference for the winter PNA interaction model incorporating centred DJF Niño-3.4, preceding March–July PDO, and their interaction ($n = 45$).

3.5. Summer-to-winter persistence and the 2026 predictor range

The historical relationship between developing-season JJA and subsequent DJF Niño-3.4 anomalies showed strong positive persistence across the 44 completed developing years from 1982 to 2025 (Figure 6a). Nevertheless, individual events varied widely around the fitted regression, indicating that similar summer SST anomalies did not necessarily produce similar winter intensities. For example, the 1997 and 2015 events exhibited nearly identical JJA anomalies (+1.34 and +1.37 °C, respectively), but their subsequent DJF anomalies differed appreciably (+1.98 and +2.40 °C). Conversely, the 1982 event developed from a considerably weaker JJA anomaly (+0.58 °C) before reaching +2.11 °C in the following winter. These contrasts show that summer Niño-3.4 conditions inform subsequent winter intensity but do not uniquely determine its magnitude. The expanding-window hindcasting procedure described in Section 2.7 yielded an out-of-sample coefficient of determination of $R^2_{\mathrm{EW}} = 0.74$ across 29 sequential evaluations for 1997–2025 (Eq. 9). This result indicates that the linear persistence model reproduced a substantial proportion of the observed interannual variability in subsequent winter Niño-3.4 anomalies within the historical evaluation period. However, the hindcast skill reflects performance under the range of ENSO conditions represented in the historical record and does not independently establish predictive reliability for unprecedented developing-season anomalies. The historical JJA Niño-3.4 predictors ranged from −1.66 to +1.37 °C, whereas the observed JJA 2026 anomaly reached +2.12 °C (Figure 6b). The 2026 value therefore exceeded the historical maximum by 0.75 °C, corresponding to a normalized extrapolation distance of $\delta = 0.25$ relative to the full historical calibration range (Eq. 11). This places the 2026 event outside the predictor domain used to estimate and evaluate the summer-to-winter persistence relationship, despite the comparatively strong historical hindcast performance.

Applying the regression calibrated on all 44 historical pairs to the JJA 2026 anomaly produced a nominal DJF Niño-3.4 estimate of +2.99 °C, with a conventional 95% prediction interval of +1.69 to +4.29 °C (Eq. 10; Fig 6a). These values represent the conditional extrapolation of the fitted linear relationship

rather than an independently validated prediction of winter 2026/27. In particular, the interval accounts for uncertainty under the assumed regression model but does not incorporate potential changes in the persistence relationship outside the historical predictor range. The combined hindcasting and predictor-domain assessment therefore identify an important distinction between historical predictive skill and extrapolation reliability. Although the summer-to-winter relationship exhibits substantial skill within the evaluated historical sample, the exceptional JJA 2026 anomaly extends beyond the conditions under which that skill was established. Consequently, neither the nominal winter estimate nor its conventional prediction interval can be interpreted as a calibrated forecast for DJF 2026/27.

Figure 6. Historical summer-to-winter Niño-3.4 persistence and assessment of the 2026 predictor domain. (a) Relationship between developing-year JJA and subsequent DJF Niño-3.4 anomalies for 44 completed years (1982–2025), showing the fitted linear regression and conventional 95% prediction band. The expanding-window hindcast performance ($R^2_{\mathrm{EW}} = 0.74$) was evaluated over 29 developing years (1997–2025). The orange symbol indicates the regression extrapolation for JJA 2026 (+2.12 °C), with a nominal DJF estimate of +2.99 °C and a conventional 95% prediction interval of +1.69 to +4.29 °C. (b) Distribution of historical JJA Niño-3.4 anomalies and the observed 2026 value, highlighting its exceedance of the historical maximum (+1.37 °C) by 0.75 °C. The normalised extrapolation distance is $\delta = 0.25$.

3.6. Robustness of the winter Niño-3.4–PNA relationship

The stability of the concurrent winter Niño-3.4–PNA association was evaluated using the event-exclusion and circular moving-block bootstrap procedures described in Section 2.6.5. Excluding DJF 1991/92, the winter following the Mount Pinatubo eruption, produced a negligible change in the correlation coefficient, from $r = 0.562$ for the complete 45-winter sample to $r = 0.556$ for the remaining 44 winters (Figure 7a). This limited sensitivity indicates that the positive historical association was not driven by the inclusion of this potentially influential winter. However, the exclusion test does not isolate the eruption's climatic effects or rule out other influential observations. The circular moving-block bootstrap further supported the stability of the positive association under alternative assumptions about short-range temporal dependence (Figure 7b; Table S4). For the complete sample, the percentile-based 95% confidence intervals ranged from 0.358–0.731 with two-year blocks to 0.411–0.721 with five-year blocks. Following exclusion of DJF 1991/92, the corresponding intervals were 0.338–0.728 and 0.399–0.718. All eight confidence intervals, obtained using block lengths of two to five years for both sample configurations, remained entirely above zero. The smallest lower confidence bound was 0.338, indicating that the positive correlation persisted across the examined resampling specifications. The sensitivity analyses show that the historical winter Niño-3.4–PNA correlation remains positive after excluding DJF 1991/92 and across the tested bootstrap block lengths. These findings support the robustness of the association reported in Section 3.4 but do not provide evidence of significant PDO modulation. The bootstrap results quantify uncertainty in the historical concurrent relationship; they do not establish causality or confirm that the association will remain stable under the exceptional Pacific conditions observed in 2026.

Figure 7. Sensitivity and sampling uncertainty of the concurrent winter Niño-3.4–PNA association. (a) Pearson correlations for the complete 45-winter sample (1982–2026; $r = 0.562$) and after excluding DJF 1991/92 ($n = 44$; $r = 0.556$). (b) Percentile-based 95% confidence intervals obtained from circular moving-block bootstrap resampling of paired annual Niño-3.4 and PNA observations, using block lengths of two to five years and 10,000 replicates per configuration. Results are shown for both the complete and reduced samples.

4. Discussion

4.1. Exceptional ENSO development and the North Pacific background state

The 2026 event showed two distinctive characteristics: exceptionally rapid intensification of tropical Pacific SST anomalies and coexistence with a strongly negative PDO state. The March–August Niño-3.4 increase was the largest observed during 1982–2026 at +2.52 °C, while the JJA anomaly reached +2.12 °C. Unlike the completed high-amplitude events of 1982/83, 1997/98, and 2015/16, the 2026 event developed under substantially negative North Pacific conditions, with a March–July PDO mean of −1.53. The July 2026 combination of Niño-3.4 above +2.0 °C and PDO below -1.5 was absent from the preceding 531 paired monthly observations. These findings establish that the developing event occupied a joint Pacific climate state not represented in the available historical record, rather than merely exhibiting an unusually large Niño-3.4 anomaly. The contrasting historical development trajectories highlight the limitations of interpreting rapid spring–summer warming as an indicator of subsequent winter intensity. The 1982 event intensified substantially after August, whereas the 2015 event developed from comparatively warm spring conditions. Such differences are consistent with the role of upper-ocean heat content, thermocline feedback, wind forcing, and seasonal phase locking in controlling ENSO evolution (Chen et al., 2015; Takahashi & Dewitte, 2016; Timmermann et al., 2018). Because these processes were not explicitly resolved, the exceptional 2026 development rate cannot independently establish the event's eventual amplitude or persistence.

The negative PDO conditions accompanying the 2026 warming provide important context for the broader Pacific climate state. The PDO reflects extratropical ocean–atmosphere variability influenced by both North Pacific processes and tropical Pacific forcing through atmospheric teleconnections (Newman et al., 2016; Zhao et al., 2021; Di Lorenzo et al., 2023). Consequently, the observed ENSO–PDO configuration should not be interpreted as evidence of two independent climatic forcings. The weak positive historical correlation between Niño-3.4 and PDO ($r = 0.27$) indicates limited overall linear covariability, but does not preclude individual episodes with strongly contrasting index signs. Moreover, the concentration of high-amplitude Niño-3.4 observations within a small number of historical events limits the effective sample available for characterising extreme joint states. The principal implication is therefore the distinction between historical joint-state novelty and dynamical novelty. The 2026 configuration was unrepresented in the observed paired record, but its absence from earlier observations does not establish a new ENSO regime, a distinct physical mechanism, or a recurrence probability. Nevertheless, this configuration provides a scientifically relevant case for examining whether historical ENSO–circulation relationships remain informative under Pacific background conditions poorly represented by previous high-amplitude events.

4.2. ENSO–circulation relationships and the role of PDO

The most consistent atmospheric relationship identified in this study was the positive association between Niño-3.4 and winter PNA. Developing-year JJA and SON Niño-3.4 anomalies were correlated with subsequent winter PNA at $r = 0.55$ and $r = 0.59$, respectively, while the concurrent DJF correlation was $r = 0.56$. All three associations remained significant after dependence-aware permutation testing and false-discovery-rate adjustment. In contrast, the corresponding NAO and AO correlations were weak and statistically nonsignificant. This geographical contrast is consistent with the established importance of tropical Pacific heating for North Pacific and North American circulation, including the excitation of large-scale atmospheric wave responses (Scaife et al., 2017; Yeh et al., 2018; Taschetto et al., 2020). However, the index-based analysis does not directly resolve the associated Rossby wave structure, tropical heating distribution, or atmospheric energy propagation.

The difference between monthly and winter-targeted correlations further emphasizes the importance of temporal sampling in ENSO teleconnection analysis. Monthly lead–lag correlations reached approximately +0.22 when PNA followed Niño-3.4 by two to three months, whereas winter-targeted correlations were substantially stronger. This contrast is consistent with the seasonality of ENSO teleconnections, which depend on the evolving atmospheric basic state and the seasonal sensitivity of extratropical circulation to tropical forcing. Nevertheless, seasonal averaging, the restriction to DJF circulation, and differences in the composition of the monthly and seasonal samples also affect the estimated correlations. The positive monthly lag maxima should therefore be interpreted as statistical temporal associations rather than estimates of physical propagation times or evidence of a specific causal sequence. The winter Niño-3.4–PNA association also remained stable under the sensitivity procedures examined. Exclusion of DJF 1991/92 changed the concurrent correlation only marginally, from 0.562 to 0.556, while all moving-block bootstrap confidence intervals remained above zero for block lengths of two to five years. These findings indicate that the selected potentially influential winter did not drive the positive association and that it was insensitive to the tested short-range dependence specifications. Nevertheless, the concurrent correlation corresponds to approximately 32% shared linear variance, leaving substantial winter PNA variability unexplained by Niño-3.4 alone. Internal atmospheric variability, the spatial characteristics of tropical forcing, and other circulation influences may contribute to this residual variability, although the present analysis cannot quantify their individual roles.

A central question was whether the developing-season PDO state modifies the historical winter Niño-3.4–PNA relationship. The PDO-stratified correlations were positive under both background states, with $r = 0.62$ for positive PDO and $r = 0.51$ for non-positive PDO. However, the formal interaction coefficient was small relative to its uncertainty ($\beta_3 = 0.0488$, HAC $p = 0.174$), providing no statistically significant evidence of a PDO-dependent change in the regression slope. The positive conditional Niño-3.4 coefficient ($\beta_1 = 0.2984$, $p < 0.001$) indicates that the winter ENSO–PNA association remained detectable after accounting for PDO and the interaction term. The historical rarity of the 2026 Niño-3.4–PDO configuration does not necessarily indicate a change in atmospheric teleconnections. Previous studies have examined PDO-dependent ENSO influences on regional temperature and precipitation (Maher et al., 2022), whereas the present analysis tests whether PDO modifies the winter Niño-3.4–PNA relationship. The nonsignificant interaction does not exclude potential PDO influences, particularly under

very strong ENSO conditions or through nonlinear and spatially varying responses. Rather, it indicates that the 45-winter sample provides insufficient statistical evidence for linear PDO modulation of the Niño-3.4–PNA relationship. The results confirm a robust historical ENSO–PNA association but provide no statistically significant evidence that the negative PDO conditions accompanying the 2026 event will strengthen or weaken the subsequent winter PNA response. This distinction matters when assessing whether established historical relationships apply to the developing event, particularly under an unusual Pacific background state.

4.3. Historical persistence, predictive skill, and extrapolation uncertainty

The summer-to-winter Niño-3.4 analysis revealed substantial historical persistence, with an expanding-window hindcast coefficient of determination of $R^2_{\mathrm{EW}} = 0.74$ across 29 evaluations. This result indicates that a relatively simple linear model captured much of the interannual variation in subsequent winter anomalies within the historical evaluation period. Nevertheless, contrasting trajectories of major historical events show that similar summer anomalies can precede substantially different winter outcomes. The persistence relationship therefore represents a statistical tendency rather than a deterministic description of ENSO evolution. The exceptional 2026 summer anomaly introduces an additional limitation that is not captured by conventional hindcast performance. Historical JJA predictors ranged from −1.66 to +1.37 °C, whereas the 2026 value reached +2.12 °C, exceeding the calibration maximum by 0.75 °C. The corresponding normalized extrapolation distance of $\delta = 0.25$ indicates that the predictor lies one-quarter of the historical calibration range beyond its upper boundary. Thus, although the model showed substantial historical skill, the 2026 predictor falls in a region where its statistical relationship with subsequent winter intensity has not been empirically evaluated. Extrapolation of the fitted regression yielded a nominal DJF anomaly of +2.99 °C, with a conventional 95% prediction interval of +1.69 to +4.29 °C. These values are mathematically consistent with the estimated linear relationship but depend on its continuation beyond the historical predictor domain. The prediction interval accounts for residual variability and parameter uncertainty under the assumed regression structure; it does not account for possible structural changes in ENSO persistence at unusually high amplitudes. Consequently, do not interpret the nominal estimate as a calibrated winter forecast, and do not assign the conventional 95% coverage interpretation to the interval for the 2026 event.

This distinction is physically relevant because ENSO evolution involves state-dependent ocean–atmosphere coupling, nonlinear thermocline feedback, and variations in tropical convection (Dommenget et al., 2013; Cai et al., 2015; Takahashi & Dewitte, 2016; Timmermann et al., 2018). These processes may influence whether exceptionally strong summer warming persists, intensifies, or weakens during subsequent months. However, the present analysis does not establish that a particular nonlinear mechanism will operate during 2026, nor does it demonstrate a breakdown of the historical linear relationship. The broader methodological implication is that strong retrospective predictive performance does not guarantee reliability under unprecedented predictor conditions. Expanding-window validation reduces temporal information leakage and provides a more defensible assessment of historical predictive performance than an in-sample fit. Nevertheless, it cannot validate a model in an unsampled region of predictor space. The explicit predictor-domain assessment therefore adds an essential qualification to the

interpretation of historical ENSO persistence, particularly when exceptionally large developing-season anomalies are used to infer subsequent winter conditions.

4.4. Implications for North American winter hydroclimate

The observed ENSO–PNA relationship may affect North American winter hydroclimate because PNA-related circulation variability influences the distribution of atmospheric temperature anomalies, storm tracks, and precipitation. Across western Canada and the northwestern United States, these atmospheric conditions can affect precipitation phase, seasonal snow accumulation, snowmelt timing, and runoff generation (Fleming & Whitfield, 2010; Whitfield et al., 2010; Bonsal et al., 2017; Dierauer et al., 2019). However, the resulting hydrological response is spatially heterogeneous and depends on the interaction between large-scale circulation and regional catchment characteristics.

The strong relationship between developing-season Niño-3.4 and subsequent winter PNA indicates that tropical Pacific conditions contain historical information about winter circulation variability. Nevertheless, this statistical association does not establish the realised PNA state for winter 2026/27. Furthermore, a given PNA index value does not uniquely determine regional temperature or precipitation anomalies, particularly where atmospheric circulation patterns differ in spatial structure or interact with other modes of variability. The absence of gridded circulation and surface-climate analyses therefore prevents direct attribution of regional meteorological conditions to the relationships identified here. The weak Niño-3.4 associations with NAO and AO also require careful interpretation. Their nonsignificant correlations indicate limited linear relationships within the temporal windows and index definitions considered, rather than an absence of all Pacific influences on North Atlantic or Arctic circulation. Such influences may depend on atmospheric pathways, background states, and temporal evolution not resolved by seasonal index correlations (Jiménez-Esteve & Domeisen, 2018; Domeisen et al., 2019; Hardiman et al., 2019). From a hydrological perspective, atmospheric teleconnections influence flood and water-resource conditions through intermediate processes rather than through direct index-to-discharge relationships. Changes in winter temperature and precipitation can alter snow accumulation, rain–snow partitioning, antecedent moisture, and the timing of meltwater delivery. Whether these changes increase or decrease streamflow or flood potential depends on basin elevation, storage, regulation, soil conditions, and the coincidence of precipitation and snowmelt. Because these variables were not analysed, the present results cannot establish the magnitude, direction, or probability of hydrological anomalies during winter 2026/27. The findings therefore provide a large-scale circulation context for subsequent regional hydroclimatic assessment, rather than a direct prediction of North American precipitation, snowpack, or flooding.

4.5. Methodological limitations and uncertainty

Several limitations constrain the interpretation and generalisability of the results. First, the effective historical sample is particularly limited at high ENSO amplitudes. Although the Niño-3.4–PDO phase-space analysis includes 538 paired monthly observations, consecutive values are temporally dependent, and strong anomalies are concentrated within a small number of episodes. Therefore, the absence of historical observations in the 2026 phase-space sector cannot be interpreted as evidence of a statistically

unprecedented population-level event. Similarly, the 45-winter circulation sample provides limited information for detecting interactions that may occur only under extreme ENSO or PDO conditions.

Second, the analysis relies on climate indices that summarise complex spatial fields into scalar measures. Niño-3.4 does not resolve the longitudinal distribution of tropical SST anomalies or convective heating, while PDO, PNA, NAO, and AO do not fully characterize the spatial structure of their associated oceanic and atmospheric variability. Consequently, physically distinct climate configurations may yield similar index values, and the inferred statistical relationships cannot uniquely identify the mechanisms driving atmospheric circulation anomalies. Third, the correlation and regression analyses primarily describe linear relationships. Although circular-shift inference, block permutations, HAC covariance estimation, and moving-block bootstrap procedures address selected forms of temporal dependence and sampling uncertainty, they do not eliminate possible confounding, nonstationarity, or nonlinear interactions. The event-exclusion analysis similarly evaluates sensitivity to one potentially influential winter without controlling for all sources of internal or externally forced climate variability.

Fourth, the expanding-window hindcast evaluates historical prediction performance but does not validate the persistence model beyond the observed JJA predictor range. The conventional prediction interval also depends on linear-regression assumptions whose applicability cannot be established for the exceptional 2026 anomaly. The extrapolation assessment quantifies the distance from the calibration domain but does not provide a probabilistic measure of model failure or structural uncertainty. Finally, the observational cutoff limits the prospective interpretation. The 2026 climate-index values were preliminary, the five-consecutive-three-month ENSO duration criterion had not yet been satisfied, and winter 2026/27 remained unobserved. Accordingly, the study cannot establish the eventual event classification, mature-winter intensity, or realized atmospheric circulation response.

4.6. Prospective assessment of winter 2026/27

The subsequent evolution of the 2026 event offers an opportunity to assess whether historical ENSO persistence and circulation relationships apply under a Pacific climate configuration poorly represented in the available record. Once winter 2026/27 observations become available, the realized DJF Niño-3.4 anomaly can be compared with the historical persistence relationship, while the corresponding PNA index can be evaluated against the observed ENSO–PNA association. These comparisons should distinguish two separate questions: whether the exceptional summer Niño-3.4 anomaly evolves consistently with historical summer-to-winter persistence, and whether the realized winter circulation is consistent with the historical conditional ENSO–PNA relationship. Agreement with either relationship would support its continued applicability in this case, whereas substantial departures would motivate further examination of ocean–atmosphere coupling, the spatial distribution of tropical heating, internal atmospheric variability, and the North Pacific background state. A single winter, however, cannot independently establish the presence or absence of systematic PDO modulation. Further investigation requires gridded atmospheric circulation, tropical convection, temperature, and precipitation data, alongside coupled-model experiments to distinguish ENSO forcing from internal variability and background-state effects. Assessing regional hydrological impacts would also require snowpack, soil moisture, and streamflow observations integrated with catchment-scale analyses.

The combined evidence points to an exceptional 2026 event with an unusual development and joint Pacific background state, while the historical ENSO–PNA relationship remains statistically supported without detectable linear PDO modulation. The main uncertainty is whether these historical relationships transfer to a developing event whose summer Niño-3.4 anomaly lies outside the calibration domain. The study therefore provides a quantitative observational benchmark for evaluating winter 2026/27, while maintaining a necessary distinction between historical statistical evidence, model extrapolation, and future climatic outcomes.

5. Conclusions

This study provides a prospective assessment of the developing 2026 El Niño using six climate indices and observations available through August 2026. By evaluating its evolution against historical ENSO–PDO configurations, winter circulation relationships, and summer-to-winter persistence, the analysis identifies three principal findings.

First, the 2026 event showed the fastest March–August Niño-3.4 intensification in the 45-year observational record, increasing by +2.52 °C at a linear rate of +0.51 °C month^{-1}. This increase exceeded that of 1997 by 0.41 °C. The event also developed under a markedly negative PDO state, with a March–July mean of −1.53. No observation in the paired monthly record before 2026 combined a three-month Niño-3.4 anomaly above +2.0 °C with PDO below −1.5. This combination places the developing event in an exceptional position within the historical sample, without indicating a distinct dynamical regime or determining its eventual winter intensity.

Second, PNA exhibited the strongest and most consistent historical association with Niño-3.4 among the circulation indices examined. Correlations with winter PNA were 0.55, 0.59, and 0.56 for developing-year JJA, SON, and concurrent DJF Niño-3.4, respectively, and remained significant after dependence-aware testing and multiple-comparison adjustment. The concurrent relationship was robust to exclusion of DJF 1991/92 and alternative moving-block bootstrap specifications. In contrast, NAO and AO associations were not statistically significant, and the regression analysis did not detect significant modulation of the winter Niño-3.4–PNA slope by developing-season PDO (HAC $p = 0.174$). The limited number of high-amplitude events, however, constrains inference about background-state interactions.

Third, historical summer-to-winter ENSO persistence exhibited substantial hindcast skill but could not be validated for the exceptional 2026 conditions. The expanding-window regression achieved $R^2_{\mathrm{EW}} = 0.74$ across 29 hindcasts, whereas the 2026 JJA Niño-3.4 anomaly exceeded the historical calibration maximum by 0.75 °C ($\delta = 0.25$). The resulting nominal DJF estimate of +2.99 °C, with a conventional 95% prediction interval of +1.69 to +4.29 °C, therefore, represents an extrapolation rather than a calibrated winter forecast. This distinction highlights the limitations of transferring historical predictive skill to climatic conditions outside the observed predictor domain.

Overall, the findings establish an exceptional developing ENSO–PDO configuration while confirming a statistically supported historical ENSO–PNA association without detectable linear PDO modulation. The study provides a quantitative benchmark for evaluating the realised winter 2026/27 Niño-3.4 and PNA conditions. Determining whether the historical relationships remain applicable under this unusual Pacific

state, and assessing any associated regional hydroclimatic consequences, will require subsequent winter observations, spatial atmospheric analyses, and hydrological data.

Data and code availability

The six climate-index records are publicly available from NOAA (State of the Ocean climate-index archive, NOAA/CPC and NOAA/PSL) and the University of Washington. We retrieved the data in September 2026 from the NOAA State of the Ocean climate-index archive (https://stateoftheocean.osmc.noaa.gov/). The processed monthly and seasonal series and the analysis code, including the seeded permutation and bootstrap procedures, are available at https://doi.org/10.5281/zenodo.23285724

Funding

This research was supported by the Natural Sciences and Engineering Research Council of Canada (NSERC) through a Discovery Grant (RGPIN-2026-05029).

Declaration of competing interest

The authors declare no competing financial or personal interests.

CRediT authorship contribution statement

Fatemeh Moradi: Methodology, Software, Formal analysis, Investigation, Validation, Visualization, Writing – original draft. **Hossein Bonakdari:** Conceptualization, Supervision, Funding acquisition, Writing – review & editing.

Declaration of Generative AI and AI-assisted technologies in the scientific writing process

The current study employed AI tools for passage checking and grammatical revision. We guarantee the content's validity, and its accuracy has been verified by human expertise.

References

Barnston, A. G., & Livezey, R. E. (1987). Classification, seasonality and persistence of low-frequency atmospheric circulation patterns. *Monthly Weather Review*, *115*(6), 1083–1126. https://doi.org/10.1175/1520-0493(1987)115<1083:CSAPOL>2.0.CO;2

Barnston, A. G., Tippett, M. K., Ranganathan, M., & L'Heureux, M. L. (2019). Deterministic skill of ENSO predictions from the North American Multimodel Ensemble. *Climate Dynamics*, *53*(12), 7215–7234. https://doi.org/10.1007/s00382-017-3603-3

Benjamini, Y., & Hochberg, Y. (1995). Controlling the false discovery rate: A practical and powerful approach to multiple testing. *Journal of the Royal Statistical Society: Series B*, *57*(1), 289–300. https://doi.org/10.1111/j.2517-6161.1995.tb02031.x

Bonsal, B. R., Cuell, C., Wheaton, E., Sauchyn, D. J., & Barrow, E. (2017). An assessment of historical and projected future hydro-climatic variability and extremes over southern watersheds in the Canadian Prairies. *International Journal of Climatology*, *37*(10), 3934–3948. https://doi.org/10.1002/joc.4967

Cai, W., Santoso, A., Wang, G., Yeh, S.-W., An, S.-I., Cobb, K. M., Collins, M., Guilyardi, E., Jin, F.-F., Kug, J.-S., Lengaigne, M., McPhaden, M. J., Takahashi, K., Timmermann, A., Vecchi, G., Watanabe, M., & Wu, L. (2015). ENSO and greenhouse warming. *Nature Climate Change*, *5*(9), 849–859. https://doi.org/10.1038/nclimate2743

Capotondi, A., McGregor, S., McPhaden, M. J., Cravatte, S., Holbrook, N. J., Imada, Y., Sanchez, S. C., Sprintall, J., Stuecker, M. F., Ummenhofer, C. C., Zeller, M., Farneti, R., Graffino, G., Hu, S., Karnauskas, K. B., Kosaka, Y., Kucharski, F., Mayer, M., Qiu, B., … Xu, T. (2023). Mechanisms of tropical Pacific decadal variability. *Nature Reviews Earth & Environment*, *4*(11), 754–769. https://doi.org/10.1038/s43017-023-00486-x

Chen, D., Lian, T., Fu, C., Cane, M. A., Tang, Y., Murtugudde, R., Song, X., Wu, Q., & Zhou, L. (2015). Strong influence of westerly wind bursts on El Niño diversity. *Nature Geoscience*, *8*(5), 339–345. https://doi.org/10.1038/ngeo2399

Deser, C., Simpson, I. R., McKinnon, K. A., & Phillips, A. S. (2017). The Northern Hemisphere extratropical atmospheric circulation response to ENSO: How well do we know it and how do we evaluate models accordingly? *Journal of Climate*, *30*(13), 5059–5082. https://doi.org/10.1175/jcli-d-16-0844.1

Deser, C., Simpson, I. R., Phillips, A. S., & McKinnon, K. A. (2018). How well do we know ENSO's climate impacts over North America, and how do we evaluate models accordingly? *Journal of Climate*, *31*(13), 4991–5014. https://doi.org/10.1175/jcli-d-17-0783.1

Di Lorenzo, E., Xu, T., Zhao, Y., Newman, M., Capotondi, A., Stevenson, S., Amaya, D. J., Anderson, B. T., Ding, R., Furtado, J. C., Joh, Y., Liguori, G., Lou, J., Miller, A. J., Navarra, G., Schneider, N., Vimont, D. J., Wu, S., & Zhang, H. (2023). Modes and mechanisms of Pacific decadal-scale variability. *Annual Review of Marine Science*, *15*, 249–275. https://doi.org/10.1146/annurev-marine-040422-084555

Dierauer, J. R., Allen, D. M., & Whitfield, P. H. (2019). Snow drought risk and susceptibility in the western United States and southwestern Canada. *Water Resources Research*, *55*(4), 3076–3091. https://doi.org/10.1029/2018wr023229

Domeisen, D. I. V., Garfinkel, C. I., & Butler, A. H. (2019). The teleconnection of El Niño Southern Oscillation to the stratosphere. *Reviews of Geophysics*, *57*(1), 5–47. https://doi.org/10.1029/2018RG000596

Dommenget, D., Bayr, T., & Frauen, C. (2013). Analysis of the non-linearity in the pattern and time evolution of El Niño Southern Oscillation. *Climate Dynamics*, *40*(11–12), 2825–2847. https://doi.org/10.1007/s00382-012-1475-0

Fleming, S. W., & Whitfield, P. H. (2010). Spatiotemporal mapping of ENSO and PDO surface meteorological signals in British Columbia, Yukon, and southeast Alaska. *Atmosphere-Ocean*, *48*(2), 122–131. https://doi.org/10.3137/ao1107.2010

Hardiman, S. C., Dunstone, N. J., Scaife, A. A., Smith, D. M., Ineson, S., Lim, J., & Fereday, D. (2019). The impact of strong El Niño and La Niña events on the North Atlantic. *Geophysical Research Letters*, *46*(5), 2874–2883. https://doi.org/10.1029/2018GL081776

Hoell, A., Hoerling, M., Eischeid, J., Wolter, K., Dole, R., Perlwitz, J., Xu, T., & Cheng, L. (2016). Does El Niño intensity matter for California precipitation? *Geophysical Research Letters*, *43*(2), 819–825. https://doi.org/10.1002/2015gl067102

Jiménez-Esteve, B., & Domeisen, D. I. V. (2018). The tropospheric pathway of the ENSO–North Atlantic teleconnection. *Journal of Climate*, *31*(11), 4563–4584. https://doi.org/10.1175/jcli-d-17-0716.1

Johnson, N. C., & Kosaka, Y. (2016). The impact of eastern equatorial Pacific convection on the diversity of boreal winter El Niño teleconnection patterns. *Climate Dynamics*, *47*(12), 3737–3765. https://doi.org/10.1007/s00382-016-3039-1

Khodri, M., Izumo, T., Vialard, J., Janicot, S., Cassou, C., Lengaigne, M., Mignot, J., Gastineau, G., Guilyardi, E., Lebas, N., Robock, A., & McPhaden, M. J. (2017). Tropical explosive volcanic eruptions can trigger El Niño by cooling tropical Africa. *Nature Communications*, *8*, 778. https://doi.org/10.1038/s41467-017-00755-6

Kim, J.-W., Yeh, S.-W., & Chang, E.-C. (2014). Combined effect of El Niño-Southern Oscillation and Pacific Decadal Oscillation on the East Asian winter monsoon. *Climate Dynamics*, *42*(3–4), 957–971. https://doi.org/10.1007/s00382-013-1730-z

Künsch, H. R. (1989). The jackknife and the bootstrap for general stationary observations. *Annals of Statistics*, *17*(3), 1217–1241. https://doi.org/10.1214/aos/1176347265

L'Heureux, M. L., Tippett, M. K., & Barnston, A. G. (2015). Characterizing ENSO coupled variability and its impact on North American seasonal precipitation and temperature. *Journal of Climate*, *28*(10), 4231–4245. https://doi.org/10.1175/jcli-d-14-00508.1

L'Heureux, M. L., Takahashi, K., Watkins, A. B., Barnston, A. G., Becker, E. J., Di Liberto, T. E., Gamble, F., Gottschalck, J., Halpert, M. S., Huang, B., Mosquera-Vásquez, K., & Wittenberg, A. T. (2017). Observing and predicting the 2015/16 El Niño. *Bulletin of the American Meteorological Society*, *98*(7), 1363–1382. https://doi.org/10.1175/bams-d-16-0009.1

L'Heureux, M. L., Tippett, M. K., Takahashi, K., Barnston, A. G., Becker, E. J., Bell, G. D., Di Liberto, T. E., Gottschalck, J., Halpert, M. S., Hu, Z., Johnson, N. C., Xue, Y., & Wang, W. (2019). Strength outlooks for the El Niño–Southern Oscillation. *Weather and Forecasting*, *34*(1), 165–175. https://doi.org/10.1175/waf-d-18-0126.1

Maher, N., Kay, J. E., & Capotondi, A. (2022). Modulation of ENSO teleconnections over North America by the Pacific decadal oscillation. *Environmental Research Letters*, *17*(11), 114005. https://doi.org/10.1088/1748-9326/ac9327

Mantua, N. J., Hare, S. R., Zhang, Y., Wallace, J. M., & Francis, R. C. (1997). A Pacific interdecadal climate oscillation with impacts on salmon production. *Bulletin of the American Meteorological Society*, *78*(6), 1069–1079. https://doi.org/10.1175/1520-0477(1997)078<1069:APICOW>2.0.CO;2

Nalley, D., Adamowski, J., Biswas, A., Gharabaghi, B., & Hu, W. (2019). A multiscale and multivariate analysis of precipitation and streamflow variability in relation to ENSO, NAO and PDO. *Journal of Hydrology*, *574*, 288–307. https://doi.org/10.1016/j.jhydrol.2019.04.024

Newey, W. K., & West, K. D. (1987). A simple, positive semi-definite, heteroskedasticity and autocorrelation consistent covariance matrix. *Econometrica*, *55*(3), 703–708. https://doi.org/10.2307/1913610

Newey, W. K., & West, K. D. (1994). Automatic lag selection in covariance matrix estimation. *Review of Economic Studies*, *61*(4), 631–653. https://doi.org/10.2307/2297912

Newman, M., Alexander, M. A., Ault, T. R., Cobb, K. M., Deser, C., Di Lorenzo, E., Mantua, N. J., Miller, A. J., Minobe, S., Nakamura, H., Schneider, N., Vimont, D. J., Phillips, A. S., Scott, J. D., & Smith, C. A. (2016). The Pacific Decadal Oscillation, revisited. *Journal of Climate*, *29*(12), 4399–4427. https://doi.org/10.1175/jcli-d-15-0508.1

Patricola, C. M., O'Brien, J. P., Risser, M. D., Rhoades, A. M., O'Brien, T. A., Ullrich, P. A., Stone, D. A., & Collins, W. D. (2020). Maximizing ENSO as a source of western US hydroclimate predictability. *Climate Dynamics*, *54*(1–2), 351–372. https://doi.org/10.1007/s00382-019-05004-8

Reynolds, R. W., Rayner, N. A., Smith, T. M., Stokes, D. C., & Wang, W. (2002). An improved in situ and satellite SST analysis for climate. *Journal of Climate*, *15*(13), 1609–1625. https://doi.org/10.1175/1520-0442(2002)015<1609:AIISAS>2.0.CO;2

Ropelewski, C. F., & Jones, P. D. (1987). An extension of the Tahiti–Darwin Southern Oscillation Index. *Monthly Weather Review*, *115*(9), 2161–2165. https://doi.org/10.1175/1520-0493(1987)115<2161:AEOTTS>2.0.CO;2

Santoso, A., McPhaden, M. J., & Cai, W. (2017). The defining characteristics of ENSO extremes and the strong 2015/2016 El Niño. *Reviews of Geophysics*, *55*(4), 1079–1129. https://doi.org/10.1002/2017rg000560

Scaife, A. A., Comer, R. E., Dunstone, N. J., Knight, J. R., Smith, D. M., MacLachlan, C., Martin, N., Peterson, K. A., Rowlands, D., Carroll, E. B., Belcher, S., & Slingo, J. (2017). Tropical rainfall, Rossby waves and regional winter climate predictions. *Quarterly Journal of the Royal Meteorological Society*, *143*(702), 1–11. https://doi.org/10.1002/qj.2910

Takahashi, K., & Dewitte, B. (2016). Strong and moderate nonlinear El Niño regimes. *Climate Dynamics*, *46*(5–6), 1627–1645. https://doi.org/10.1007/s00382-015-2665-3

Tan, X., Gan, T. Y., & Shao, D. (2016). Wavelet analysis of precipitation extremes over Canadian ecoregions and teleconnections to large-scale climate anomalies. *Journal of Geophysical Research: Atmospheres*, *121*(24), 14469–14486. https://doi.org/10.1002/2016JD025533

Taschetto, A. S., Ummenhofer, C. C., Stuecker, M. F., Dommenget, D., Ashok, K., Rodrigues, R. R., & Yeh, S.-W. (2020). ENSO atmospheric teleconnections. In M. J. McPhaden, A. Santoso, & W. Cai (Eds.), *El Niño Southern Oscillation in a changing climate* (pp. 311–335). Wiley. https://doi.org/10.1002/9781119548164.ch14

Timmermann, A., An, S.-I., Kug, J.-S., Jin, F.-F., Cai, W., Capotondi, A., Cobb, K. M., Lengaigne, M., McPhaden, M. J., Stuecker, M. F., Stein, K., Wittenberg, A. T., Yun, K.-S., Bayr, T., Chen, H.-C., Chikamoto, Y., Dewitte, B., Dommenget, D., Grothe, P., … Zhang, X. (2018). El Niño–Southern Oscillation complexity. *Nature*, *559*, 535–545. https://doi.org/10.1038/s41586-018-0252-6

Tippett, M. K., & L'Heureux, M. L. (2020). Low-dimensional representations of Niño 3.4 evolution and the spring persistence barrier. *npj Climate and Atmospheric Science*, *3*, 24. https://doi.org/10.1038/s41612-020-0128-y

Whan, K., & Zwiers, F. (2017). The impact of ENSO and the NAO on extreme winter precipitation in North America in observations and regional climate models. *Climate Dynamics*, *48*(5–6), 1401–1411. https://doi.org/10.1007/s00382-016-3148-x

Whitfield, P. H., Moore, R. D., Fleming, S. W., & Zawadzki, A. (2010). Pacific Decadal Oscillation and the hydroclimatology of western Canada—review and prospects. *Canadian Water Resources Journal / Revue Canadienne Des Ressources Hydriques*, *35*(1), 1–28. https://doi.org/10.4296/cwrj3501001

Wilks, D. S. (2016). "The stippling shows statistically significant grid points": How research results are routinely overstated and overinterpreted, and what to do about it. *Bulletin of the American Meteorological Society*, *97*(12), 2263–2273. https://doi.org/10.1175/bams-d-15-00267.1

Yeh, S.-W., Cai, W., Min, S.-K., McPhaden, M. J., Dommenget, D., Dewitte, B., Collins, M., Ashok, K., An, S.-I., Yim, B.-Y., & Kug, J.-S. (2018). ENSO atmospheric teleconnections and their response to greenhouse gas forcing. *Reviews of Geophysics*, *56*(1), 185–206. https://doi.org/10.1002/2017rg000568

Zhao, Y., Newman, M., Capotondi, A., Di Lorenzo, E., & Sun, D. (2021). Removing the effects of tropical dynamics from North Pacific climate variability. *Journal of Climate*, *34*(23), 9249–9265. https://doi.org/10.1175/JCLI-D-21-0344.1

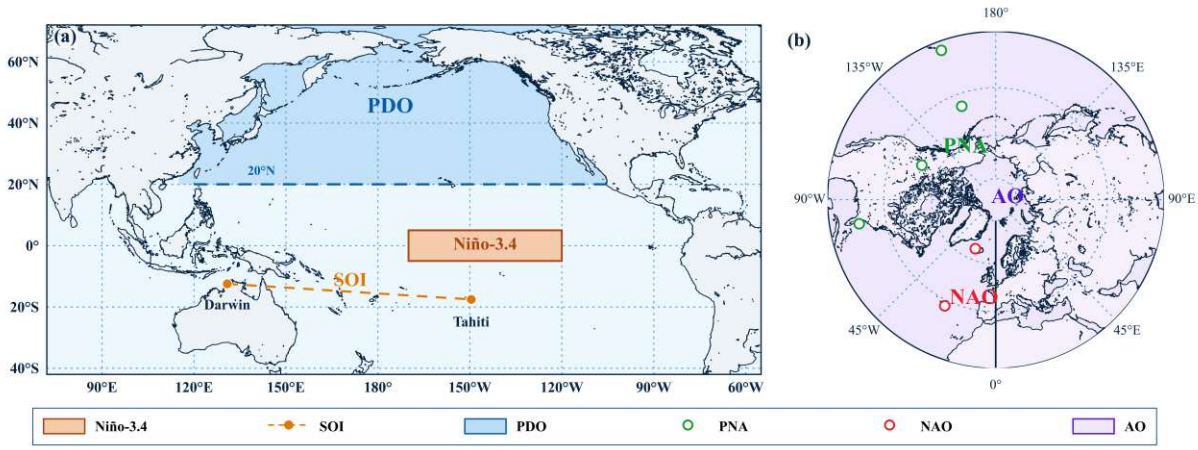


Figure 1. Geographical overview of six large-scale climate indices: (a) Niño-3.4, SOI, and PDO; (b) PNA, NAO, and AO. Shaded areas and markers indicate representative domains and reference locations.

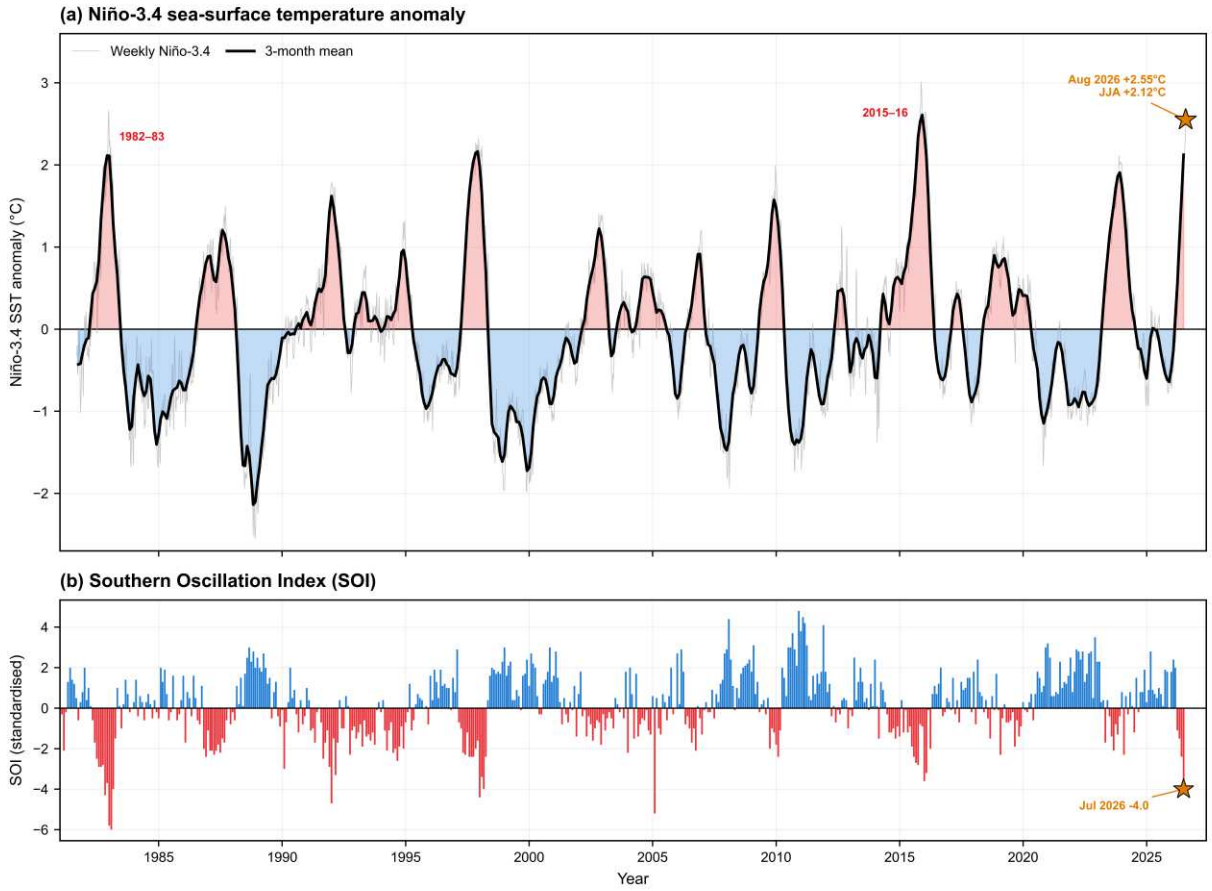


Figure 2. Historical evolution of tropical Pacific oceanic and atmospheric indices through August 2026. (a) Weekly Niño-3.4 anomalies (grey), centred three-month means (black), and positive and negative anomaly shading (red and blue, respectively). Labelled winters are those whose DJF-mean Niño-3.4 anomaly reached +2.0 °C (1982/83 and 2015/16); the 1997/98 event, whose peak three-month mean exceeded +2.0 °C but whose DJF mean was +1.98 °C, is not labelled. (b) Monthly SOI, with positive and negative values distinguished by blue and red shading. Orange stars indicate the latest available monthly observations: August 2026 for Niño-3.4 (+2.55 °C) and July 2026 for SOI (−4.0). The latest available centred Niño-3.4 mean corresponds to JJA 2026 (+2.12 °C).

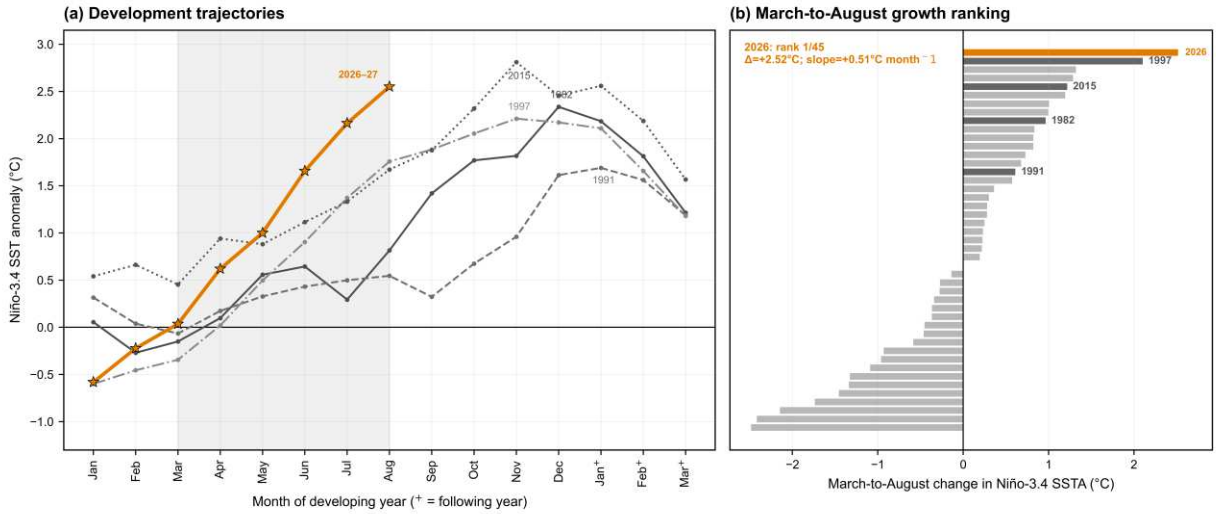


Figure 3. March–August Niño-3.4 development in 2026 relative to selected historical El Niño events. (a) Monthly Niño-3.4 anomalies for developing years 1982, 1991, 1997, 2015, and 2026. The shaded interval identifies March–August, used to quantify event development. Historical trajectories extend through the following March, whereas the 2026 record ends in August. (b) March–August Niño-3.4 anomaly changes for 1982–2026 (45 years), with selected reference years highlighted. The annotation identifies the 2026 empirical rank, net anomaly increase, and fitted six-month development slope.

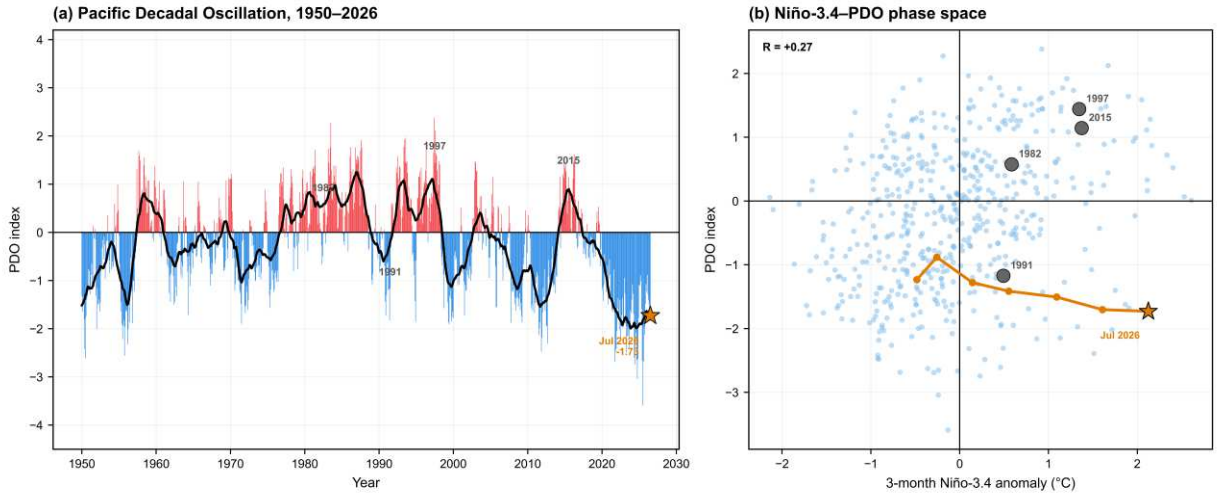


Figure 4. North Pacific background variability and historical Niño-3.4–PDO phase space. (a) Monthly PDO from 1950 to July 2026 and its centered 25-month running mean. The orange star indicates July 2026 (PDO = −1.73). (b) Joint distribution of concurrent monthly PDO and centred three-month Niño-3.4 anomalies for October 1981–July 2026 ($n = 538$; Pearson $r = 0.27$). Historical reference Julys are identified in grey, while the orange trajectory represents January–July 2026, terminating at Niño-3.4 = +2.12 °C and PDO = −1.73. The high-amplitude, negative-PDO sector Ω_{2026} is defined by Niño-3.4 greater than +2.0 °C and PDO below −1.5. No paired monthly observation before 2026 fell into this sector.

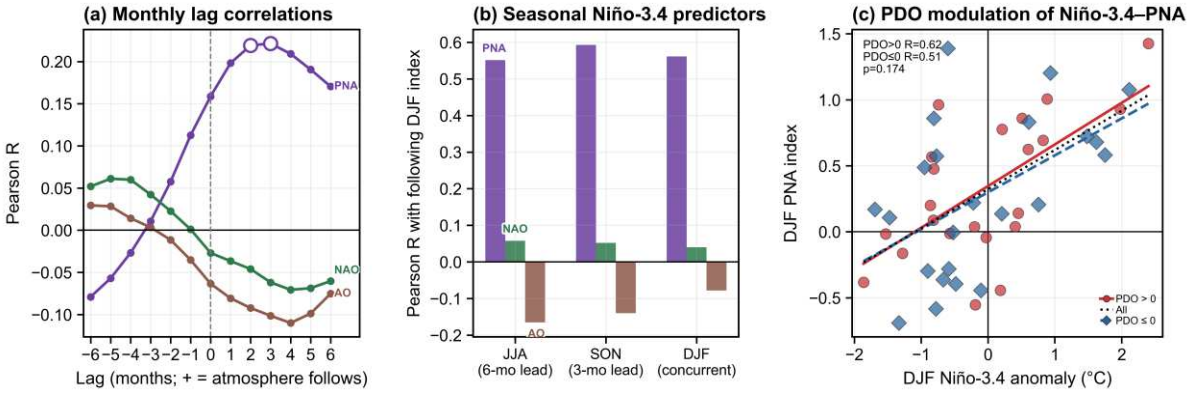


Figure 5. Monthly and seasonal Niño-3.4 relationships with Northern Hemisphere atmospheric circulation and developing-season PDO. (a) Pearson correlations between the trailing three-month Niño-3.4 mean and PNA, NAO, and AO at lags from −6 to +6 months. Positive lags indicate that atmospheric circulation follows Niño-3.4; open symbols identify correlations significant after circular-shift inference and false-discovery-rate adjustment ($q < 0.05$). (b) Correlations between developing-year JJA ($n = 44$), SON ($n = 45$), and concurrent DJF ($n = 45$) Niño-3.4 anomalies and winter circulation indices. (c) Winter Niño-3.4–PNA relationships stratified by the sign of preceding March–July PDO, with subgroup correlations and the HAC interaction-test probability indicated.

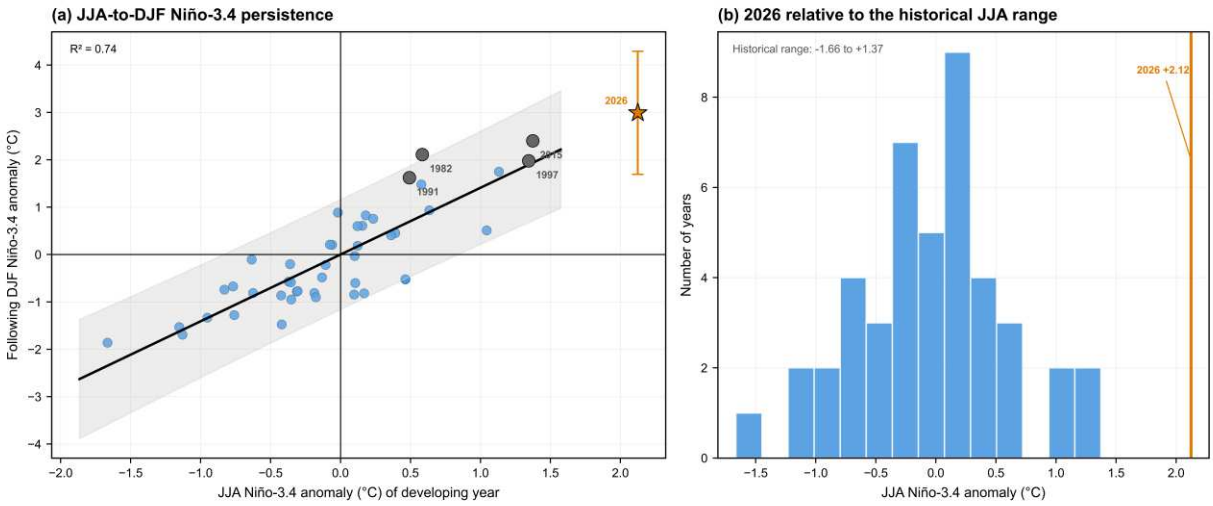


Figure 6. Historical summer-to-winter Niño-3.4 persistence and assessment of the 2026 predictor domain. (a) Relationship between developing-year JJA and subsequent DJF Niño-3.4 anomalies for 44 completed years (1982–2025), showing the fitted linear regression and conventional 95% prediction band. The expanding-window hindcast performance ($R^2_{\mathrm{EW}} = 0.74$) was evaluated over 29 developing years (1997–2025). The orange symbol indicates the regression extrapolation for JJA 2026 (+2.12 °C), with a nominal DJF estimate of +2.99 °C and a conventional 95% prediction interval of +1.69 to +4.29 °C. (b) Distribution of historical JJA Niño-3.4 anomalies and the observed 2026 value, highlighting its exceedance of the historical maximum (+1.37 °C) by 0.75 °C. The normalised extrapolation distance is $\delta = 0.25$.

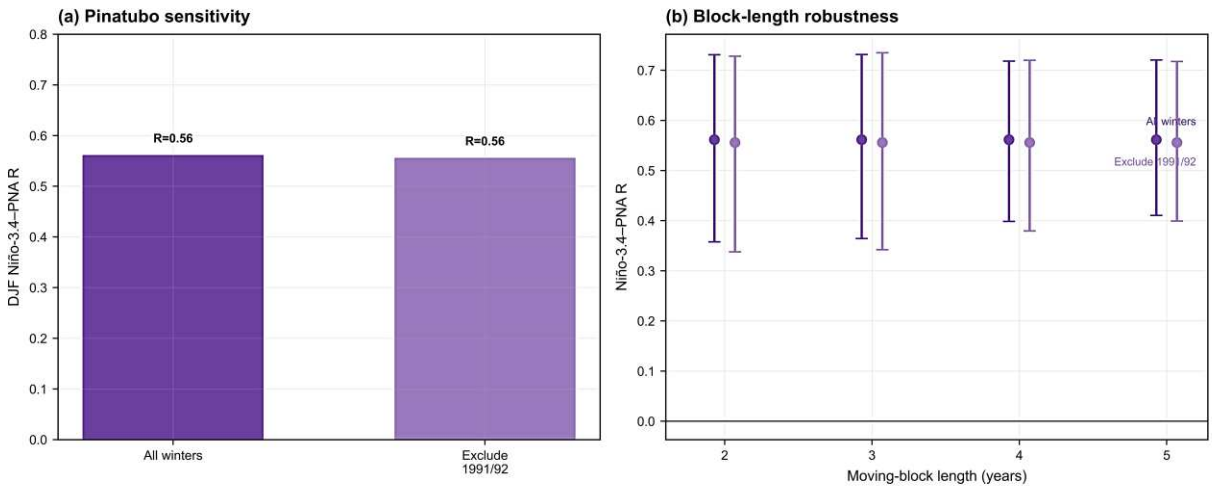


Figure 7. Sensitivity and sampling uncertainty of the concurrent winter Niño-3.4–PNA association. (a) Pearson correlations for the complete 45-winter sample (1982–2026; $r = 0.562$) and after excluding DJF 1991/92 ($n = 44$; $r = 0.556$). (b) Percentile-based 95% confidence intervals obtained from circular moving-block bootstrap resampling of paired annual Niño-3.4 and PNA observations, using block lengths of two to five years and 10,000 replicates per configuration. Results are shown for both the complete and reduced samples.

Table 1. Inventory of climate-index records used in the analysis, including their definitions, sources, native temporal resolution, and observational coverage.

Index	Definition	Source	Native resolution	Period
Niño-3.4	SST anomaly over 5° S–5° N, 170°–120° W; 1991–2020 reference period	OISST	Weekly	Sep 1981–Aug 2026
SOI	Southern Oscillation Index, based on the standardised Tahiti–Darwin pressure difference	NOAA/CPC	Monthly	Jan 1951–Jul 2026
PDO	Pacific Decadal Oscillation index	UW/JISAO	Monthly	Jan 1854–Jul 2026
PNA	Pacific–North American pattern index	NOAA/CPC	Monthly	Jan 1950–Aug 2026
NAO	North Atlantic Oscillation index	NOAA/CPC	Monthly	Jan 1950–Aug 2026
AO	Arctic Oscillation index	NOAA/CPC	Monthly	Jan 1950–Aug 2026

Note. The supplied NetCDF records identify CF-1.6 conventions. Niño-3.4 is provided at weekly resolution and converted to calendar-month means for the analysis. All remaining indices are available at monthly resolution.

Table 2. Historical reference years and the developing 2026 event considered in the analysis.

Developing year	Role in the analysis
1982	Historical very strong El Niño reference
1991	Historical comparison and Pinatubo sensitivity case
1997	Historical very strong El Niño reference
2015	Historical very strong El Niño reference
2026	Developing event evaluated at the observational cutoff

Table 3. March–August Niño-3.4 development metrics and March–July PDO background conditions for selected historical El Niño events and the developing 2026 event.

Developing year	March $N_{3.4}$ (°C)	August $N_{3.4}$ (°C)	Δ Mar–Aug (°C)	Slope (°C month^{-1})	Mar–Jul PDO
1982/83	−0.150	+0.815	+0.965	0.1572	−0.163
1997/98	−0.344	+1.758	+2.102	0.4279	+1.435
2015/16	+0.454	+1.672	+1.219	0.2143	+0.856
2026/27	+0.035	+2.551	+2.516	0.5104	−1.526

Note. The net anomaly change is defined as August minus March Niño-3.4 (Eq. 2), while the development slope is estimated by ordinary least squares using six monthly anomalies (March–August). PDO values represent the March–July mean. The 2026 values are based exclusively on observations available through August 2026; the winter 2026/27 outcome remains unobserved.

Table 4. DJF PNA, NAO, and AO statistics across study-defined winter Niño-3.4 magnitude classes for 45 completed winters (1982–2026).

Niño-3.4 class	n	PNA mean (SD)	NAO mean (SD)	AO mean (SD)
Cold	21	+0.147 (0.531)	+0.402 (0.687)	−0.178 (1.109)
Neutral	11	−0.048 (0.390)	+0.555 (0.445)	+0.388 (1.053)
Weak warm	7	+0.775 (0.316)	+0.604 (0.708)	+0.116 (0.767)
Moderate warm	1	+0.724 (—)	−1.673 (—)	−3.422 (—)
Strong warm	3	+0.731 (0.179)	+0.439 (0.652)	+0.128 (0.938)
Very strong warm	2	+1.252 (0.248)	+1.130 (0.259)	+0.082 (0.129)

Note. Classes are based on DJF-mean Niño-3.4 anomalies rather than peak three-month event amplitudes, as defined in Section 2.3. Values are class means with standard deviations in parentheses. Standard deviations are undefined for classes containing a single winter.

Table 5. DJF Niño-3.4 and atmospheric circulation indices for the three completed historical El Niño events with peak three-month Niño-3.4 anomalies of at least +2.0 °C.

Winter	DJF Niño-3.4 (°C)	DJF PNA	DJF NAO	DJF AO	Mar–Jul PDO
1982/83	+2.112	+1.077	+0.947	+0.173	−0.163
1997/98	+1.979	+0.930	−0.227	−0.778	+1.435
2015/16	+2.401	+1.427	+1.313	−0.009	+0.856
Mean	+2.164	+1.145	+0.678	−0.205	+0.709

Note. PDO represents the March–July mean preceding the corresponding winter. Events were selected according to their peak three-month Niño-3.4 anomalies. The 1997/98 event satisfies this event-level criterion despite its DJF mean being below +2.0 °C.

Table 6. Regression coefficients and HAC inference for the winter PNA interaction model incorporating centred DJF Niño-3.4, preceding March–July PDO, and their interaction ($n = 45$).

Predictor	Coefficient β	HAC SE	HAC p-value
Intercept	+0.2921	0.0720	< 0.001
DJF Niño-3.4 (centred)	+0.2984	0.0399	< 0.001
Mar–Jul PDO (centred)	−0.0038	0.0591	0.949
Niño-3.4 × PDO	+0.0488	0.0353	0.174

Note. Coefficients were estimated by ordinary least squares using 45 completed winters (1982–2026). Predictors were mean-centred before constructing the interaction term. Standard errors (SE) and two-sided p-values were calculated using the Newey–West HAC covariance estimator with a three-year truncation lag. The interaction coefficient (β_3) tests whether the winter Niño-3.4–PNA association varies with the preceding March–July PDO state.

Supplementary Files

This is a list of supplementary files associated with this preprint. Click to download.

- SupplementaryMaterialsBonakdari.docx